

Department of Physics and Astronomy
Heidelberg University

Bachelor Thesis in Physics
submitted by

Antonios Kontopoulos

born in Athens (Greece)

Towards the first observation of the leptonic
 $B^+ \rightarrow \mu^+ \nu_\mu e^+ e^-$ decay

This Bachelor Thesis has been carried out by Antonios Kontopoulos at the
Physikalisches Institut in Heidelberg
under the supervision of
Prof.Dr. Hansmann-Menzemer

Abstract

The emission of a photon in the decays $B^+ \rightarrow \gamma \ell^+ \nu$ and $B^+ \rightarrow \gamma^*(\rightarrow \ell^+ \ell^-) \ell'^+ \nu$ provides valuable insights into the first inverse moment λ_B of the B meson's light-cone distribution amplitude (LCDA). This parameter plays a vital role in QCD factorization schemes for accurately calculating non-leptonic B meson decays. A better understanding of the leading LCDA is essential for minimizing uncertainties in continuum QCD computations of B-meson matrix elements, particularly form factors and nonleptonic decays of B mesons [1].

In this thesis, the expected number of reconstructed $B^+ \rightarrow \mu^+ \nu_\mu e^+ e^-$ events are calculated relative to the $B^+ \rightarrow K^+ J/\psi(e^+ e^-)$ decay. The data was collected by the LHCb experiment from pp collisions during Run 2 in the years between 2016 and 2018, with an integrated luminosity of 5.4 fb^{-1} and a center-of-mass-energy of $\sqrt{s} = 13 \text{ TeV}$. This work represents the first steps toward the measurement of this decay, which has not been observed previously. The focus of this thesis is on the selection and study of a suitable normalization channel. The expected number of reconstructed events, $N_{\mu\nu ee}$, in the m_{ee} range of [600,1000] MeV and M_{corr} range of [5200,5800] MeV is found to be 30 ± 7 events. This result gives hope for the potential first observation, but a detailed study of the background contributions is required to confirm this.

Zusammenfassung

Die Emission eines Photons in den Zerfällen $B^+ \rightarrow \gamma \ell^+ \nu$ und $B^+ \rightarrow \gamma^*(\ell^+ \ell^-) \ell'^+ \nu$ liefert wertvolle Erkenntnisse über das erste inverse Moment λ_B der Lichtkegelverteilungsamplitude (LCDA) des B-Mesons. Dieser Parameter spielt eine entscheidende Rolle in QCD-Faktorisierungsschemata zur genauen Berechnung von nicht-leptonischen B-Meson-Zerfällen. Ein besseres Verständnis der führenden LCDA ist wesentlich für die Minimierung von Unsicherheiten in Kontinuum-QCD-Berechnungen von B-Mesonen-Matrixelementen, insbesondere Formfaktoren und nicht-leptonische Zerfälle von B-Mesonen.

In dieser Bachelorarbeit wird die erwartete Anzahl der rekonstruierten $B^+ \rightarrow \mu^+ \nu_\mu e^+ e^-$ -Ereignisse relativ zum $B^+ \rightarrow K^+ J/\psi(e^+ e^-)$ -Zerfall berechnet. Die Daten wurden vom LHCb-Experiment aus pp-Kollisionen während des Run 2 in den Jahren 2016 bis 2018 gesammelt, mit einer integrierten Luminosität von $5,4 \text{ fb}^{-1}$ und einer Schwerpunktsenergie von $\sqrt{s} = 13 \text{ TeV}$. Diese Arbeit stellt die ersten Schritte zur Messung dieses Zerfalls dar, der bisher noch nicht beobachtet worden ist. Der Schwerpunkt dieser Arbeit liegt auf der Auswahl und Untersuchung eines geeigneten Normalisierungskanals. Die erwartete Anzahl der rekonstruierten Ereignisse, $N_{\mu\nu ee}$, im m_{ee} -Bereich von $[600, 1000] \text{ MeV}$ und M_{corr} -Bereich von $[5200, 5800] \text{ MeV}$ beträgt 30 ± 7 Ereignisse. Dieses Ergebnis lässt auf eine mögliche Erstbeobachtung hoffen, aber eine detaillierte Untersuchung der Hintergrundbeiträge ist erforderlich, um dies zu bestätigen.

Contents

1	Introduction	5
2	Theoretical Background	7
2.1	Standard Model of Particle Physics	7
2.1.1	Fundamental Forces	7
2.1.2	Higgs Field	9
2.2	Flavor Physics	10
3	Motivation	11
3.1	The $\mathbf{B}^+ \rightarrow \mu^+ \nu_\mu \gamma$ decay	11
3.2	The $\mathbf{B}^+ \rightarrow \mu^+ \nu e^+ e^-$ decay	12
4	Experimental Setup	13
4.1	The LHC accelerator	13
4.2	The LHCb detector	15
4.2.1	Tracking	17
4.2.2	Magnet	20
4.2.3	Particle identification systems	21
4.2.4	Trigger	26
5	Monte Carlo Simulation	29
5.1	Effective Hamiltonian	29
5.2	Matrix elements	30
5.2.1	Virtual photon emission from the u quark of the B meson	30
5.2.2	Virtual photon emission from b quark of the B meson	30
5.2.3	Virtual photon emission from the lepton in final state	31
5.3	Monte Carlo parametrisation	32
5.4	Development of the Monte Carlo	33
6	Analysis strategy	34
6.1	Signal estimation technique	34
6.2	Corrected mass	36
7	Data processing	38
7.1	Online selection	38
7.2	Data stripping	39

7.2.1	Bremsstrahlung in the dielectron pair	39
7.3	Preselection	40
8	Analysis	43
8.1	Signal channel	43
8.1.1	Dielectron mass	43
8.1.2	\mathbf{B}^+ mass calculation	44
8.2	Reference channel	46
8.2.1	Dilepton mass measurement	46
8.2.2	\mathbf{B}^+ invariant mass measurement	46
8.2.3	Data fit	48
8.3	Results	51
9	Discussion	52

Chapter 1

Introduction

"[...] ο κόσμος ο μικρός, ο Μέγας!"¹. This is the last line in the poem "το Δοξαστικόν"² of the poem collection "Άξιον εστί"³, written by greek poet Odysseas Elytis, who was awarded the Nobel Prize in Literature in 1979. Though the line was written as a celebration of the small things in life, I find its interpretation from a particle physicist's point of view equally exciting. Our world is constructed out of various small pieces interacting with each other. Objects orders of magnitude smaller than anything our senses can understand, dictate the laws that govern the universe and are key to our modern understanding of it. Particle physics is the study that aims to shine a light, both figuratively and literally, on this "small, Great world" and through years of both theoretical and experimental work, has created a theory, the Standard Model, that accurately describes it.

This work presents a study to estimate the number of reconstructed $B^+ \rightarrow \mu^+ \nu_\mu e^+ e^-$ ⁴ events in 2016-18 Run 2 data of the LHCb experiment. This fully-leptonic rare b-decay is a window to probe the weak interaction and to set input on the first inverse moment λ_B of the B meson's light-cone distribution amplitude (LCDA), which plays an essential role in minimizing uncertainties in continuum QCD computations of B-meson matrix elements, and the Cabibbo-Kobayashi-Maskawa matrix element V_{ub} , which describes the rare transformation of a bottom quark into an up quark mediated by the weak interaction. Furthermore, the absence of hadrons in the final state of this decay allows a precise prediction.

The study is performed using data and simulation provided by the LHCb Collaboration. The LHCb experiment is one of the largest flavor physics experiments in the world, placed on the LHC beamline and it is dedicated to studying precisely B- and D-meson decays.

The number of $B^+ \rightarrow \mu^+ \nu_\mu e^+ e^-$ decays are estimated explicitly using data and Monte Carlo simulation of the reference channel $B^+ \rightarrow K^+ J/\psi(e^+ e^-)$. This reference channel has a similar final state to the signal channel but is fully reconstructable and its branching ratio is precisely known. Therefore, it can be used to estimate the amount of signal candidates

¹(eng. tr.: "[...] the small, Great world!")

²(eng. tr.: the Glorification)

³(eng. tr.: Worthy it is)

⁴Charge conjugation is implied for this work

expected in the detector, by taking into account the reference channel's efficiency and the branching ratios of the two decays. This is calculated by the equation:

$$N_{\text{sig}} = N_{\text{ref}} \cdot \frac{\mathcal{BR}(B^+ \rightarrow \mu^+ \nu_\mu e^+ e^-)}{\mathcal{BR}(B^+ \rightarrow K^+ J/\psi) \cdot \mathcal{BR}(J/\psi \rightarrow e^+ e^-)} \cdot \frac{\epsilon_{\text{sig}}}{\epsilon_{\text{ref}}},$$

where N_{sig} is the number of events in the signal, N_{ref} the number of events in the reference channel, \mathcal{BR} the branching ratio of each decay, and ϵ_{sig} and ϵ_{ref} the efficiency, for each decay.

Chapter 3 explains in detail the motivation behind the work. Chapters 2, 4 and 5 present the theoretical background and the tools used for this study, while in Chapters 6-8 the analysis work is presented. Lastly, Chapter 9 discusses the results and conclusions from this work.

For my thesis work, I joined a small team of three people that are working on the $B^+ \rightarrow \mu^+ \nu_\mu e^+ e^-$ analysis at the Physikalisches Institut. My main contributions to the analysis are detailed in Subsection 7.2.1 and Chapter 8 of this document.

Chapter 2

Theoretical Background

In this chapter, a theoretical overview of the Standard Model of particle physics (SM) and the underlying physics behind this work is presented. For a more detailed presentation of the theoretical background, the reader is referred to for example to [2].

2.1 Standard Model of Particle Physics

The SM of particle physics is the most complete theory on particle physics so far. It describes and classifies all the known elementary particles as well as the known fundamental interactions between them. Those are electromagnetism, the weak and the strong force [2].

As seen in Figure 2.1 the SM categorizes all elementary particles into the quarks, the leptons, and the gauge and scalar bosons. The quarks and leptons are called fermions and have spins of $1/2$. The fermions are further categorized into three generations of matter, each consisting of two quarks and two leptons. The bosons of the Standard Model are the force carriers for the three fundamental interactions in particle physics. Bosons are defined from their integer spin.

2.1.1 Fundamental Forces

The exchange of a spin-1 force-carrying particle known as a gauge boson, which corresponds to each of the three forces relevant to particle physics, is described by QFT. The gauge boson of QED is the photon. The force-carrying particle of the strong interaction is known as the gluon and is also massless like the photon. The charged W^+ and W^- bosons with masses $m_W \approx 80.3 \text{ GeV}$ ⁵ mediate the weak charged-current interaction, which causes nuclear β -decay and nuclear fusion. Moreover, there is a weak neutral-current interaction that is mediated by the electrically neutral Z^0 boson, with a mass $m_Z \approx 91.2 \text{ GeV}$. The relative strengths of the forces connected to the various gauge bosons are listed in Table 2.1. Although the strength of the forces depends on the scales of distance and energy being evaluated, it should be emphasized that these numbers are just suggestive.

⁵For this thesis, all quantities will be expressed in energy units without the need for additional factors such as GeV/c or GeV/c^2 . In this context, the speed of light, c , will be assumed to have a value of 1.

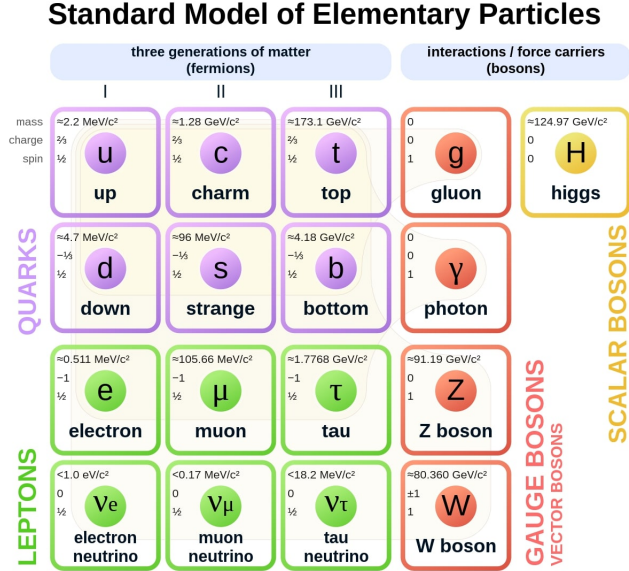


Figure 2.1: Standard Model. Figure taken from [3].

QED

On the quantum scale, the electromagnetic interaction is described by QED. All fermions described by the SM, apart from the charge-less neutrinos take part in the electromagnetic interaction. Its mediating particle is the massless photon (γ) and belongs to a $U(1)$ symmetry group. Electromagnetism has an infinite range, making it the largest range out of the three interactions of particle physics.

Weak force

The weak interaction is experienced by each of the twelve fundamental fermions. It belongs to the $SU(2) \times U(1)$ symmetry group. This symmetry is spontaneously broken by the Higgs mechanism, resulting in the massive force carrier particles Z^0 and W^\pm . Due to this phenomenon, the weak interaction's range is severely limited, being of the order of $10^{18} - 10^{16}\text{m}$ range.

The coupling with the W^\pm boson is the only known way to change quark flavor. The quantum numbers connected to the weak force are the isospin and the weak hypercharge. Moreover, under the $SU(2)$ transformations, left-handed particles are considered doublets, while right-handed singlets. This leads to the weak force only coupling to left-handed particles.

Table 2.1: Relative strength of forces: The three fundamental interactions relative to particle physics. The relative strengths are approximate indicative values for two fundamental particles at a distance of $1 \text{ fm} = 10^{-15} \text{ m}$ (roughly the radius of a proton). All numbers were taken from [2].

Force	Strength	Running coupling constant	Boson	Spin	Mass/GeV
Strong	1	1	Gluon (g)	1	0
Electromagnetism	10^{-3}	1/137	Photon (γ)	1	0
Weak	10^{-8}	10^{-6}	W boson (W^\pm)	1	80.4
			Z boson (Z^0)	1	91.2

QCD

Quantum Chromodynamics or QCD, is the QED analog for the strong interaction. It acts on particles with so-called color charge. The color charges are called "red", "blue" and "green". The quarks are the only color-charged fermions. This force is mediated by massless gluons (g), of which there are eight. The strong force follows $SU(3)$ symmetries. A unique property of the strong force is, that its force carriers, the gluons, do carry color charge, making them capable to couple with themselves.

2.1.2 Higgs Field

The Higgs boson (H) was discovered in 2012 by the ATLAS [4] and CMS [5] experiments at the Large Hadron Collider (LHC). The Higgs boson has a mass of $m_H \approx 125 \text{ GeV}$ and is a spin-0 scalar particle, contrary to the basic fermions and gauge bosons, which are spin-half and spin-1 particles, respectively. The Higgs boson, as envisioned in the Standard Model, is the only basic scalar found to date.

The Higgs boson is vital in the Standard Model as it explains how all other particles gain mass. The Higgs may be seen as an excitation of the Higgs field in QFT. In contrast to the areas associated with basic fermions and bosons, which have zero vacuum expectation values (VEV), the Higgs field is thought to have a non-zero VEV. The interaction of originally massless particles with this non-zero Higgs field gives them mass. The finding of a Higgs-like particle at the LHC is a vindication of the theoretical assumptions that comprise the SM. Lastly, the masses of the W^\pm , Z^0 , and H bosons are all in the order of 100 GeV on the electroweak scale. This is not by coincidence; the masses of the weak gauge bosons are intricately tied to the Higgs process in the Standard Model.

2.2 Flavor Physics

Flavor physics investigates, among other things, the properties and behavior of particles that are weakly interacting, i.e. quarks, and electrons. The primary goal of flavor physics is to understand the origins of the flavor structure observed in the SM.

Through flavor physics, the modern understanding of weak interaction has been shaped. It is experimentally proven that different quarks couple differently to the weak force and not universally. This motivated the principle of the separation of quark mass and flavor eigenstates. This relation can be summarized by the Cabibbo-Kobayashi-Maskawa (CKM) matrix:

$$\begin{pmatrix} d' \\ s' \\ b' \end{pmatrix} = \begin{pmatrix} V_{ud} & V_{us} & V_{ub} \\ V_{cd} & V_{cs} & V_{cb} \\ V_{td} & V_{ts} & V_{tb} \end{pmatrix} \begin{pmatrix} d \\ s \\ b \end{pmatrix}, \quad (2.1)$$

where the mass eigenstates are being denoted as $q = \{d, s, b\}$ and the weak eigenstates as $q' = \{d', s', b'\}$. The CKM matrix is by definition unitary and by convention it is formulated with a down-type vector and an up-type row-matrix parametrization respectively [2]. The probability of a flavor eigenstate i to another j through the charged current of the W boson is proportional to $|V_{ij}|^2$.

The CKM matrix absolute values have been measured at [2]:

$$\begin{pmatrix} |V_{ud}| & |V_{us}| & |V_{ub}| \\ |V_{cd}| & |V_{cs}| & |V_{cb}| \\ |V_{td}| & |V_{ts}| & |V_{tb}| \end{pmatrix} = \begin{pmatrix} 0.974 & 0.225 & 0.004 \\ 0.225 & 0.973 & 0.041 \\ 0.009 & 0.040 & 0.999 \end{pmatrix}. \quad (2.2)$$

As seen in equation 2.2 the non-diagonal values of the matrix are significantly smaller, than the diagonal ones. Because of this, the Wolfenstein parametrization of the CKM is widely used, using real-number variables λ, A, ρ and η . To $\mathcal{O}(\lambda^4)$ the CKM matrix can be rewritten as:

$$\begin{pmatrix} V_{ud} & V_{us} & V_{ub} \\ V_{cd} & V_{cs} & V_{cb} \\ V_{td} & V_{ts} & V_{tb} \end{pmatrix} = \begin{pmatrix} 1 - \lambda^2/2 & \lambda & A\lambda^3(\rho - i\eta) \\ -\lambda & 1 - \lambda^2/2 & A\lambda^2 \\ A\lambda^3(1 - \rho - i\eta) & -A\lambda^2 & 1 \end{pmatrix}, \quad (2.3)$$

with $\lambda = 0.22506 \pm 0.00050$, $A = 0.811 \pm 0.026$, $\bar{\rho} = 0.124_{-0.018}^{+0.019}$ and $\bar{\eta} = 0.356 \pm 0.011$ [6], with $\bar{\rho}$ and $\bar{\eta}$ given as:

$$\bar{\rho} = \rho(1 - \lambda^2/2), \text{ and} \quad (2.4)$$

$$\bar{\eta} = \eta(1 - \lambda^2/2). \quad (2.5)$$

Chapter 3

Motivation

To study the theoretical limits of the SM and find New Physics beyond it, direct and indirect searches are employed. Direct searches try to detect new particles, either by creating them in an accelerator or by getting them from external sources⁶. This, however, is strongly restricted by the experimental setup's energy scale. In the LHC this corresponds to several TeV. On the other hand, indirect searches can be performed through processes involving quantum loops. Within these loops, virtual particles can be produced and impact the measured observable, while being heavier than the energy scale in the process.

3.1 The $B^+ \rightarrow \mu^+ \nu_\mu \gamma$ decay

Fully-leptonic $B^+ \rightarrow \mu^+ \nu_\mu$ decays are expected to have a very small branching ratio of about 4×10^{-7} , due to their branching ratios being proportional to the small $|V_{ub}|^2$ matrix element of the CKM matrix and because of helicity suppression. The neutrino's helicity and chirality coincide, effectively dictating and restricting the available helicity states of the other particles in two-body decays. This feature is suppressing the total number of $B^+ \rightarrow \mu^+ \nu_\mu$ in the detector. These fully-leptonic decays are an excellent test of the SM since, due to the absence of hadrons in the final state, their branching ratios can be theoretically predicted with good accuracy.

On the other hand, the $B^+ \rightarrow \mu^+ \nu_\mu \gamma$ decay features an additional photon that lifts the helicity suppression but is suppressed by an additional factor α_{EM} . Due to the additional photon, the prediction of the branching ratio depends on the structure-function of the B^+ meson which is parametrized at the first order by the parameter λ_B . A measurement of the $B^+ \rightarrow \mu^+ \nu_\mu \gamma$ would allow to probe of the poorly known parameter λ_B and improve the precision of the predictions of non-leptonic B-meson decays.

⁶an example are direct searches of dark matter in cosmic radiation

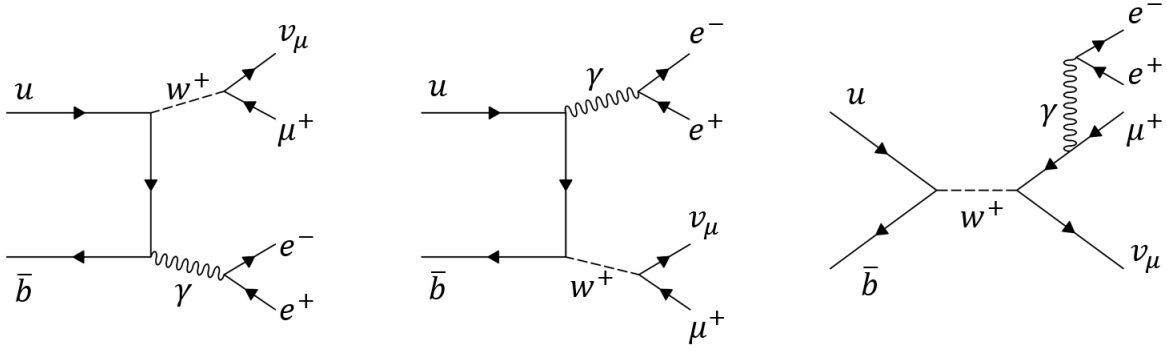


Figure 3.1: The first-order Feynmann diagrams of the $B^+ \rightarrow \mu^+ \nu_\mu e^+ e^-$ decay. By ignoring the $\gamma - e^- - e^+$ vertex one gets the first-order diagrams of the $B^+ \rightarrow \mu^+ \nu_\mu \gamma$ decay.

3.2 The $B^+ \rightarrow \mu^+ \nu_\mu e^+ e^-$ decay

From a theoretical perspective, the branching ratio of $B^+ \rightarrow \mu^+ \nu_\mu \gamma$ decay is the best channel to probe the structure-function of the B^+ and measure the λ_B parameter. Experimentally, however, this channel is difficult to study. B mesons are comparatively long-lived particles. Thus, when they are produced in the interaction point, they fly for a certain time in the detector before decaying. The point of this decay is called the secondary vertex. Consequently, the location of the secondary vertex is an important variable for this kind of study and so it must be pin-pointed using the direction of the produced particles. The limitation of locating the secondary vertex in the $B^+ \rightarrow \mu^+ \nu_\mu \gamma$ comes due to the existence of a neutrino in the final state. To the detector the neutrino is invisible, meaning it cannot be reconstructed. This means that the muon track is the only visible track in the measurement, limiting the location of the reconstructed secondary vertex of the decay as a straight line instead of a point. As a result, at least a second decay track is needed to locate the secondary vertex. Pairing to this is the fact that, the photon does not leave reconstructable tracks in the detector, but only depositions of energy in the calorimeters. These depositions cannot be direction orientated, so the position of the secondary vertex is not possible to be restricted.

To solve this issue, the study of the $B^+ \rightarrow \mu^+ \nu_\mu e^+ e^-$ decay has been employed, which is dominated by the $B^+ \rightarrow \mu^+ \nu_\mu \gamma^*$ transition, where a virtual photon goes to a dielectron pair. This decay carries a lot of similarities to its real photon counterpart, with the addition of two extra tracks, the e^\pm -tracks, making the location of the secondary vertex possible. A drawback however of this decay can be, that the dielectron pair can resonate with the ρ and ω mesons, worsening the precision of the branching ratio calculation. Figure 3.1 shows the three first-order Feynmann diagrams for the $B^+ \rightarrow \mu^+ \nu_\mu e^+ e^-$ decay.

Chapter 4

Experimental Setup

In this chapter, the detecting apparatus of the Large Hadron Collider beauty (LHCb) experiment, which is located at the French-Swiss border near Geneva at the European Organization for Nuclear Research (CERN⁷) is presented. The LHCb is one of nine experiments operated at the Large Hadron Collider (LHC) and searches for new physics beyond the SM, by studying rare decays of beauty (b) and charm (c) hadrons [7]. For a more detailed presentation of this experimental setup, the reader is referred to for example to [7, 8, 9, 10].

4.1 The LHC accelerator

The LHC with a near-circular design and a circumference of 26.7 km is the largest particle-particle accelerator in the world. It consists of two rings with superconducting magnets, that circulate in opposite directions proton (p) and lead (Pb) beams⁸, and collide them in eight interaction points. Currently⁹ nine experiments are on the LHC beamline. The largest experiments positioned on four of the interaction points are ATLAS, CMS, ALICE, and LHCb. ATLAS and CMS are considered to be general-purpose detectors. They have been built with complementary to each other technology and both of them are investigating a large spectrum of high-energy physics and new physics. ALICE focuses on heavy ion collisions (pPb and PbPb) in the study of the Quark-Gluon Plasma and matter in extreme interacting densities. Finally, the LHCb experiment investigates flavor physics, in B- and D-meson decays. Apart from these experiments the smaller experiments of the LHC are LHCf, TOTEM, MoEDAL-MAPP, FASER, and SND@LHC. More information on the LHC experiments can be found at [11, 12, 13, 14, 15, 16, 17, 18].

The LHC's maximum center-of-mass-energy is set to be at $\sqrt{s} = 14$ TeV, with a maximum luminosity for pp collisions in ATLAS and CMS of $\mathcal{L} = 10^{34}\text{cm}^{-2}\text{s}^{-1}$ [8]. During its first run of operation (Run 1), the LHC reached a maximum center-of-mass-energy at $\sqrt{s} = 8$ TeV and a peak luminosity of $\mathcal{L} = 8 \cdot 10^{33}\text{cm}^{-2}\text{s}^{-1}$, while in Run 2 these values were raised to

⁷Ed: in french "Conseil européen pour la recherche nucléaire"

⁸ATLAS, CMS, and LHCb mainly study pp collisions, while ALICE focuses more on PbPb and pPb collisions

⁹at the date of June 2023

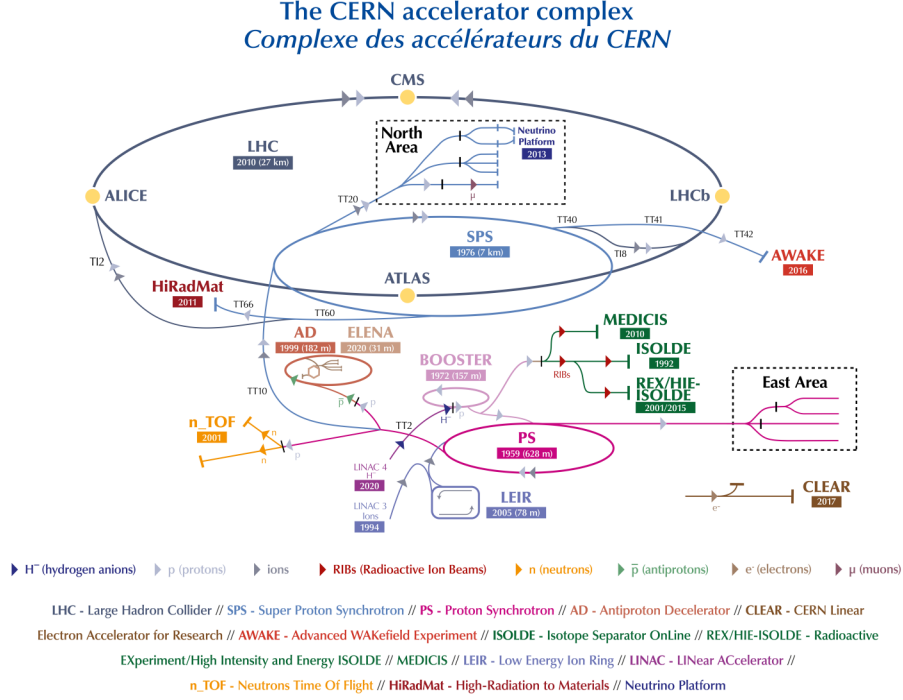


Figure 4.1: The LHC and the CERN accelerator complex [21].

$\sqrt{s} = 13$ TeV and $\mathcal{L} = 1 - 2 \cdot 10^{34} \text{cm}^{-2}\text{s}^{-1}$ [19]. In this work all data and MC simulation used are in the Run 2 framework for the years 2016-18, with LHCb-specific integrated luminosity of 5.4fb^{-1} and a center-of-mass-energy of $\sqrt{s} = 13$ TeV [20].

Figure 4.1 gives an overview of the accelerator complex, to which the LHC belongs. Hydrogen atoms¹⁰ are ejected into the LINAC 4 linear accelerator and accelerated up to an energy of 160 MeV, where they pass over into the Proton Synchrotron Booster (PBS). During this process the atoms are stripped of their electrons, leaving pure proton beams into the accelerator beamline. These protons are then accelerated up to 2 GeV, before being ejected into the Proton Synchrotron (PS), so they can reach an energy of 26 GeV. After this step, the Super Proton Synchrotron boosts them to 450 GeV before the protons are finally transferred to the two beam pipes of the LHC.

In the LHC the two beams are being circulated in opposite directions to each other (one clockwise and the other anti-clockwise). Each LHC ring takes 4 minutes and 20 seconds to fill, and the protons require 20 minutes to reach their maximum energy of 6.5 TeV. Under typical working circumstances, beams circulate for several hours inside the LHC beam pipes, after which the luminosity starts to decrease significantly and they are discarded. The two beams collide within the four main detectors - ALICE, ATLAS, CMS, and LHCb - with a total energy of 13 TeV at the collision site [21].

¹⁰a similar procedure is followed for Pb atoms ejected in LINAC 3, with however different energy values

4.2 The LHCb detector

The LHCb detector is a single-arm forward spectrometer, with a pseudorapidity¹¹ coverage range of $1.8 < \eta < 4.9$. This corresponds to acceptance angles of 10 to 300 mrad in the bending plane relative to the beamline, and 10 to 250 mrad in the non-bending plane. Contrary to the other three large experiments of the LHC, the LHCb detector does not have a cylindrical geometry, but a forward-facing one [9]. The reason behind this asymmetric orientation is, that the produced b- and c- hadrons are boosted in the forward direction. The main mechanism that brings forth such particles is gluon-gluon fusion. Considering the distribution of gluons within a proton, which mostly carries a small fraction of the proton's momentum, the most probable scenario for quark pair production occurs at the parton level via a low-x-value¹² gluon interaction with another gluon carrying a sufficiently large amount of momentum to provide the energy required for the formation of a heavier quark. This can be also observed in Figure 4.2.

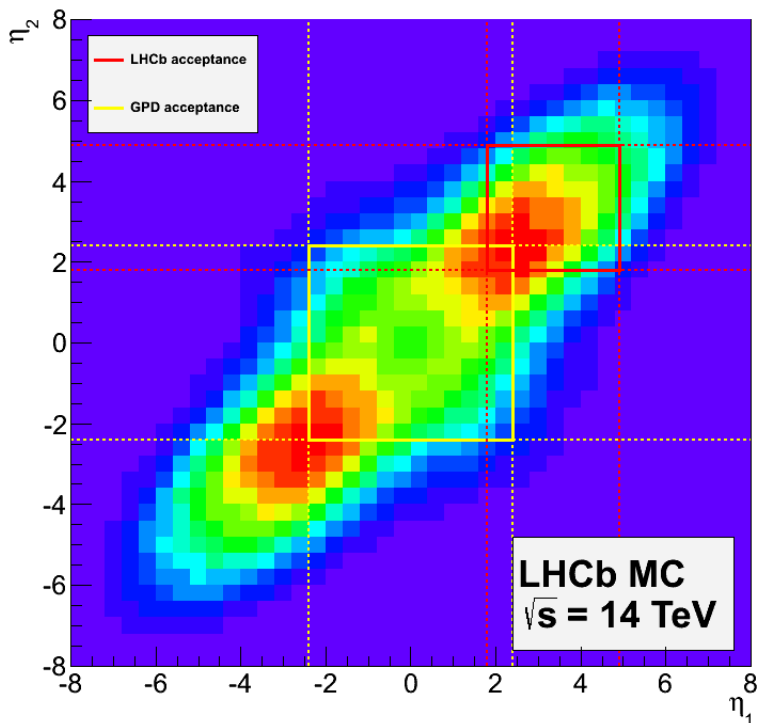


Figure 4.2: Pseudorapidity distributions of $b\bar{b}$ as produced in the LHC. The red box signifies the acceptance of the LHCb detector, while the yellow the acceptance of a detector with cylindrical geometry. The plot is generated using MC simulation for Run 2. The Figure is taken from [22].

¹¹where $\eta = -\log[\tan(\frac{\theta}{2})]$, for θ the polar angle with respect to the beam direction

¹²where x the Bjorken x [2]

The LHCb uses a right-handed coordinate system with z defined along the beam axis into the detector (downstream), y vertical, and x horizontal - pointing towards the center of the accelerator ring. Along the z -axis, the following sub-detectors are positioned:

- the Vertex Locator (VELO) around the collision point ($z = 0$)
- the RICH1¹³
- the TT tracking station
- the warm dipole magnet
- the T1-3 tracking stations
- the RICH2
- the SPD/PS the pre-shower and scintillating pad detector
- the M1 muon station
- the ECAL electromagnetic calorimeter
- the HCAL hadronic calorimeter
- and the M2-5 muon stations.

Figure 4.3 is a graphical representation of the cross-section of the LHCb detector in Run 2.

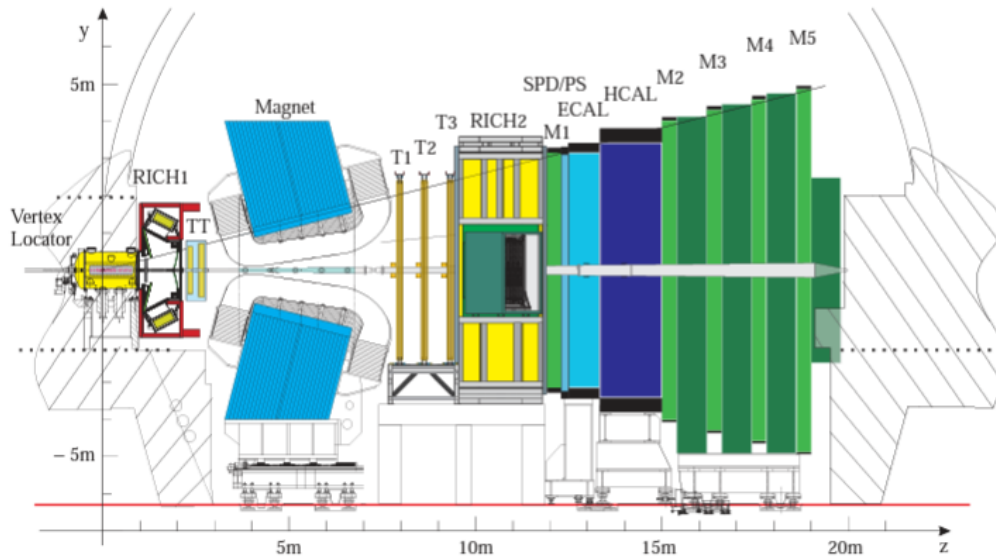


Figure 4.3: The LHCb detector in Run 2 with its sub-detectors. [23]

¹³RICH stands for Ring Imaging Cherenkov Detector

4.2.1 Tracking

The tracking capabilities of a particle detector play a major role in the resolution of the data it collects. Through tracking one can extrapolate properties like the charge of a particle, measure the momentum, and the vertex location [24]. LHCb has three types of tracking detectors: the Vertex Locator (VELO), the silicon strip detectors (TT, IT), and the drift tubes (OT). These systems reconstruct tracks with a momentum resolution of 0.5-1.0% at 200 GeV [25].

Vertex Locator (VELO)

The Vector Locator (VELO) is a tracking detector shaped like a cylindrical shell around the pp-interaction point. Its main purpose is to locate primary vertices (PV) and secondary vertices (SV)¹⁴, which are a result of b- and c- hadron decays. Secondary vertices are often displaced and thus it is necessary to have a detector measuring this dislocation, e.g. to determine the decay time of a particle.

The VELO is made out of 42 annular disks of silicon detectors stacked together¹⁵ and provides measurements for the r (R-sensors) and ϕ (Φ -sensors)¹⁶ coordinates [9]. The VELO has a diameter of 90.5 mm, a thickness of 300 μm , and a minimum distance between the strips of 40 μm , while it has a radial sensitivity region of 8 to 44 mm [25]. Finally, the VELO can be set on the detector in two different configurations, open, where the two semi-cylinders have a maximum distance of 6 cm, and closed, when the LHC beam is stable. This is done to protect it from an excess of radiation damage. Figure 4.4 is a sketch of the VELO detector.

Silicon Tracker

Silicon tracker technology is been used in two sub-detector systems, the Trigger Tracker (TT), upstream of the tracker, and the Inner Tracker (IT), downstream of it.

The TT microstrip is comprised of two separate stations positioned 30 cm apart from each other. The strip layers are in a so-called "x-u-v-x" configuration, where the x-orientation consists of the vertical strips and the u-and v-orientations signify tilted layers of the detector by $\pm 5^\circ$ relative to the x-orientation. Figure 4.5 provides a visual representation of this configuration.

The IT microstrips are located on the T1-3 stations and their configuration is the same as in the TT trackers. Figure 4.6 shows the layout of an IT detector.

The TT and IT have a single hit resolution of approximately 50 μm .

¹⁴Due to the relatively long lifetime of b-mesons, they do not instantly decay in the detector, but instead they fly in it, before decaying. The point on which this decay occurs and a vertex of decay products appears, is named secondary vertex.

¹⁵all together compose the cylindrical shell

¹⁶where r , the radius vector transverse to the beamline and ϕ the azimuthal angle of the x-y-plane in the cylinder coordinates

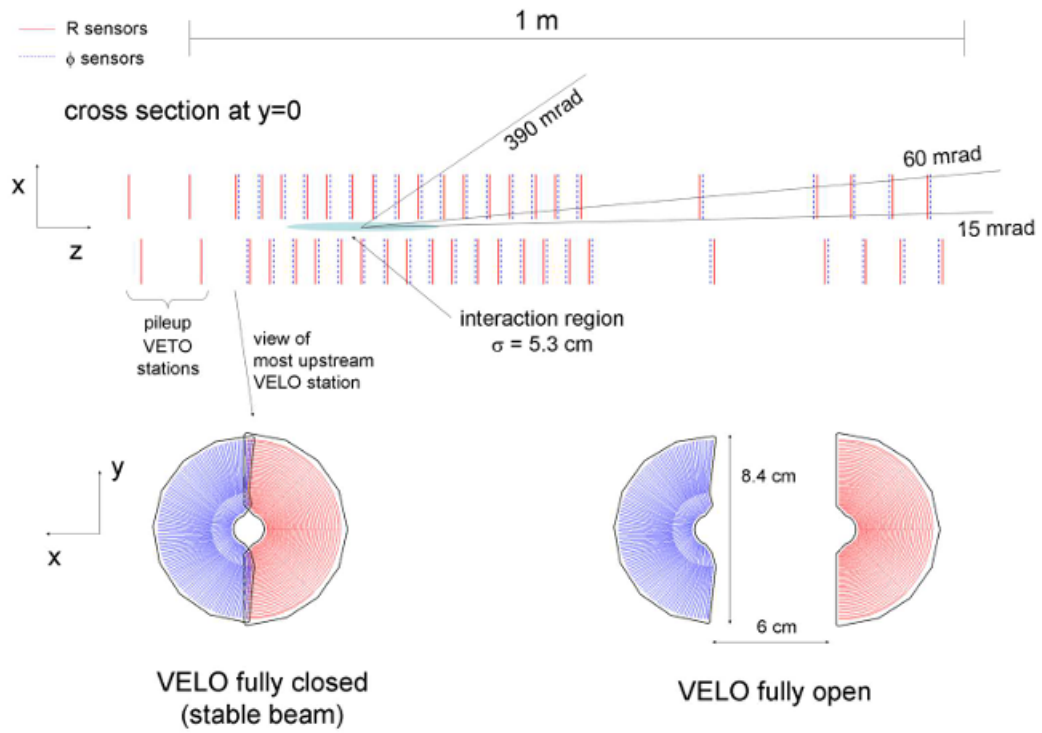


Figure 4.4: The VELO sub-detector. Figure taken from [7]

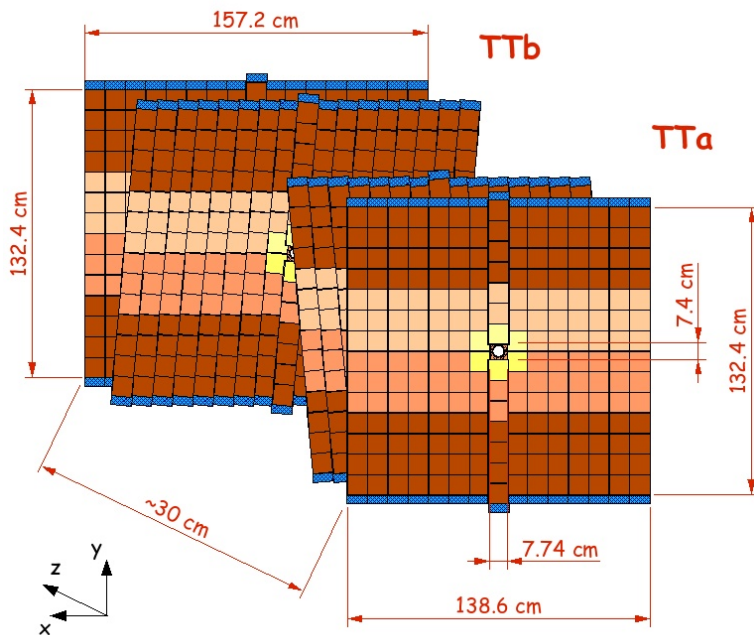


Figure 4.5: Trigger Tracker x-u-v-x configuration. Figure taken from [26].

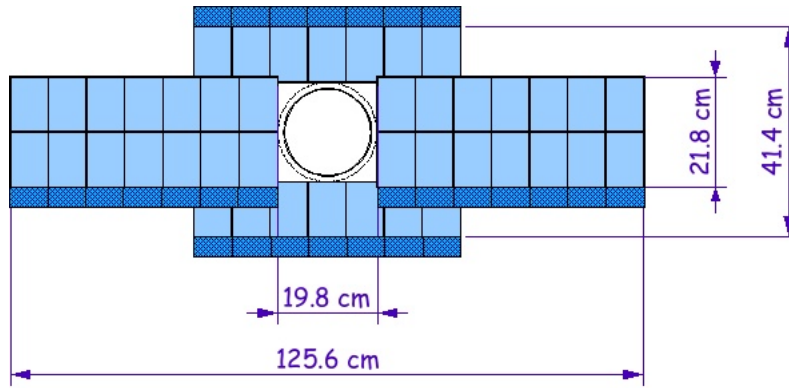


Figure 4.6: IT layout. Figure taken from [26]

Outer Tracker

The Outer Tracker (OT) covers the outer zone of the T1-3 tracking stations. Due to the lower flux of particles in that region of the detector, proportional chambers of gas-filled straw tubes are used for tracking. The gas mixture consists of Ar, CO₂ and O₂. The drift time of the detector is on the order of 50 ns. The OT tracker is configured in an x-u-v-x orientation, similar to the TT and IT trackers [27]. Figure 4.7 presents the OT layout.

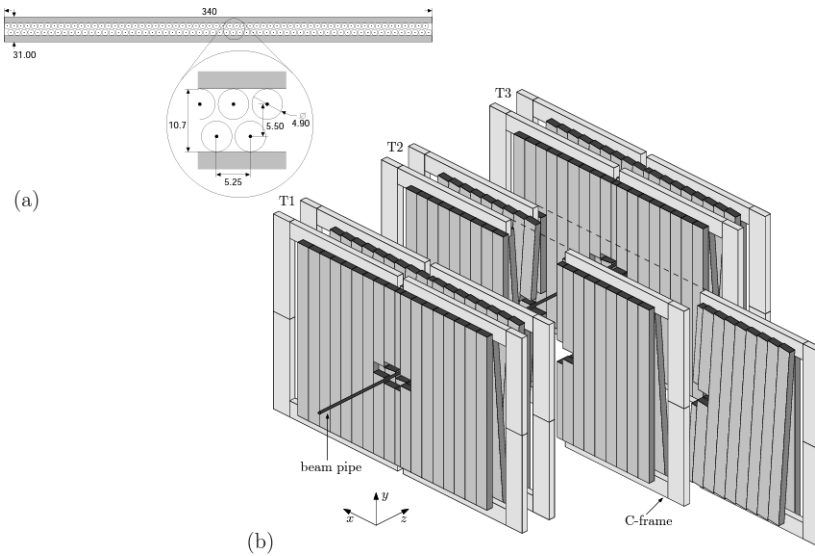


Figure 4.7: (a) Module cross section. (b) Arrangement of OT straw-tube modules in layers and stations. Figure taken from [27]

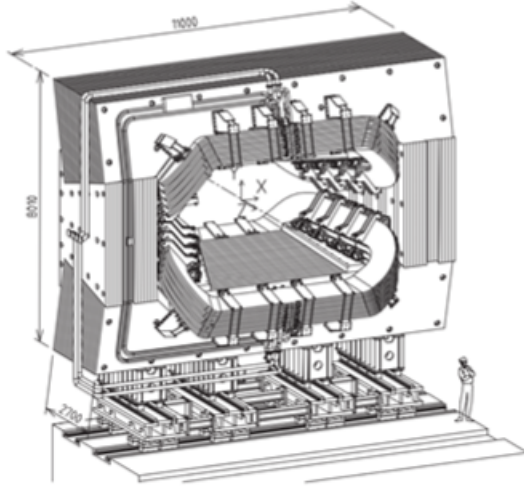


Figure 4.8: The LHCb magnet. Figure from [28].

Track reconstruction

The trajectories of the produced charged particles are reconstructed using hits from the tracking detectors described above. The tracks of greater physical importance in the analysis process are the long tracks¹⁷, for which the momentum reconstruction is the most precise. The reconstruction of these long tracks begins with identifying a straight-line trajectory in the VELO and signal from the T1-3 stations. Afterward, a consistency check with the TT signal takes place. Finally, all reconstructed tracks are fitted using a Kalman filter algorithm, which accounts for multiple scattering, energy loss, and other detector effects. The quality of the fit is determined by the reduced- χ^2 -value¹⁸ of the fitted track.

4.2.2 Magnet

The LHCb magnet is categorized as a warm dipole magnet. It consists of two coils, that provide a homogenous magnetic field of 4 Tm [28]. This causes the tracks of charged particles to bend, due to the Lorentz force, and by using the track signals upstream and downstream of the magnet derive the momentum of the passing particles [24]. It is noteworthy to point out, that for bias mitigation in data collection half of the LHCb data is taken with a MagUp orientation of the magnetic field and the other half with a MagDown orientation. Figure 4.8 depicts the LHCb magnet.

¹⁷as long tracks are defined trajectories that stimulate both the VELO and T1-3 stations. TT stimulation is optional

¹⁸ $\chi_{red}^2 = \frac{\chi^2}{n_{dof}}$, where dof stands for degrees of freedom

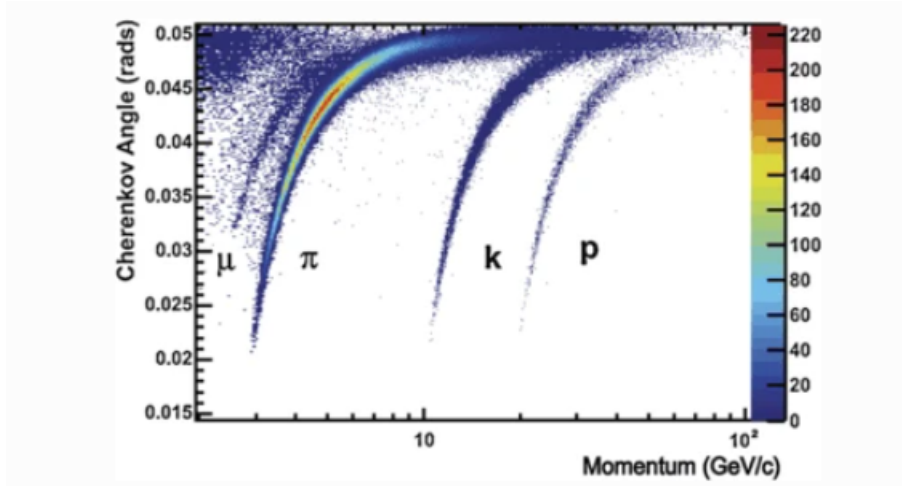


Figure 4.9: Cherenkov angle in the C_4F_{10} radiator of RICH1. Figure from [9]

4.2.3 Particle identification systems

Identifying the different types of particles (PID) in the detector is an extremely important process, which is done with the use of the RICH, calorimetry, and muon station systems.

RICH detectors

The Ring Cherenkov RICH1 and RICH2 detectors play a major role in PID in the LHCb experiment. RICH1 focuses on low-momentum particles (1–60 GeV), whereas RICH2 is tailored to particles with larger momenta (15–100 GeV). By filling the two detectors with distinct radiator materials these different momentum ranges are achieved. RICH1 employs separate aerogel and C_4F_{10} radiator, while RICH2 is filled with CF_4 radiator.

Cherenkov detectors work by utilizing the emitted light from particles passing through specific materials. When a particle travels in a medium with a velocity larger than the speed of light in that medium, then so-called Cherenkov radiation is emitted. The radiation emission is done in a cone shape, with an angle depending on the particle’s velocity. The relationship between the Cherenkov angle and the particle’s velocity is described by the following equation:

$$\cos(\theta_{ch}) = \frac{1}{n\beta}, \quad (4.1)$$

where θ_{ch} the Cherenkov angle, $\beta = \frac{v}{c}$ and n the refractive index. In Figure 4.9 a plot of the Cherenkov angle against the momentum of the LHCb experiment is depicted. The figure also shows how particles with different masses have distinct signatures for low momenta, only losing resolution on the high end of the presented spectrum [29].

In both RICH detectors, Cherenkov light is directed toward the HPDs using a combination of spherical and flat mirrors. Figure 4.10 depicts the configuration of the RICH1 detector; the RICH2 detector layout is identical but arranged in a horizontal orientation.

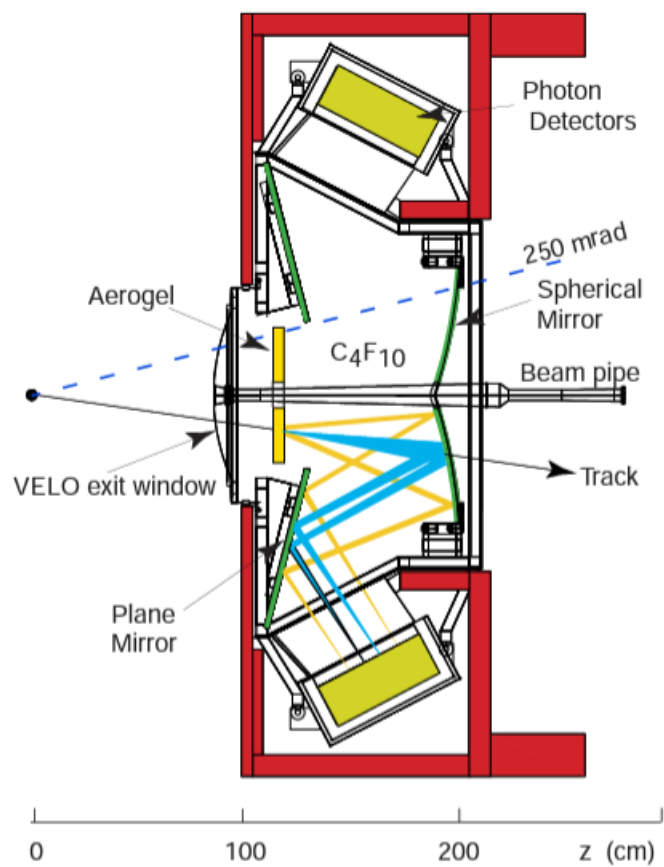


Figure 4.10: Layout of the vertical RICH1 detector. Figure from [23].

Calorimetry system

The calorimetry systems of the LHCb experiment measure the energy and position of electrons, photons, and hadrons. A signal from these subdetectors paired with the existence or lack of signal in other parts of the LHCb apparatus can indirectly parametrize the types of particles passing along a track.

The calorimetry system is located downstream from the RICH2 in between the first and the second muon station (Fig. 4.3). The calorimetry system is comprised of the Scintillating Pad Detector (SPD), the Preshower (PS), Electromagnetic (ECAL), and Hadronic calorimeters (HCAL). More details on the LHCb calorimetry system can be found at [7].

Scintillating Pad detector: The initial calorimeter layer is situated downstream of the first muon station (M1) and the RICH2 detector. It enhances the separation of electrons and photons and is crucial to the first level of the LHC trigger, which excludes events with high multiplicity by placing a cut on the number of SPD hits.

Preshower: Its primary function is to decrease the background from charged pions and is situated downstream of the SPD after a 15mm thick lead converter. It accomplishes this by utilizing the longer interaction length of hadrons, more specifically pions, compared to electrons. Additionally, the finer granularity of the PS contrasted with the ECAL allows for more effective separation of electrons and photons.

Electromagnetic calorimeter: The ECAL is a sampling calorimeter with a shashlik configuration employing a plastic scintillator as the detection material (4mm thick) and a lead as the absorber (2mm thick). Here the electron and photon energy, which are typically completely absorbed in the ECAL chamber, are measured. This energy measurement is used as well in the particle identification algorithm included in the hardware trigger to distinguish between electrons and pions. The ECAL covers a depth equivalent to 25 radiation lengths. The ECAL's energy resolution is given as:

$$\frac{\sigma_E}{E} = \frac{10\%}{\sqrt{E}} \oplus 1\% \quad (4.2)$$

for the energy given in GeV.

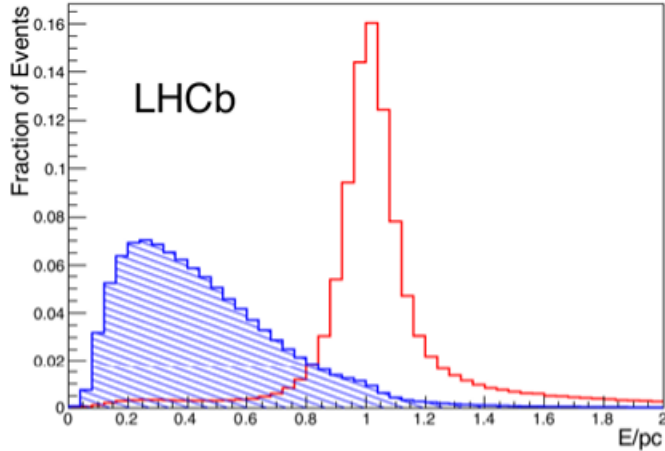


Figure 4.11: Distribution of E/pc in the ECAL for electrons (red) and hadrons (blue), obtained from data recorded in 2011. Figure from [9].

Electron identification and reconstruction: The identification of electrons in this study relies on their energy deposits in the calorimeter system as well as the presence of a track associated with the energy cluster. The ratio between energy and momentum (E/pc), measured by the calorimeter devices, plays a crucial role in discriminating electrons from other particles, as demonstrated in Fig. 4.11. The identification probability is determined either by comparing the electron and pion hypotheses using a difference of log-likelihoods (DLL) approach or by employing a neural network trained on Monte Carlo events.

Reconstructing the momentum of electrons presents challenges due to the emission of one or more Bremsstrahlung photons by the electrons upstream of the magnet. These photons may interact with the ECAL in a different cell or become lost, as depicted in Fig. 4.12. Although lost Bremsstrahlung photons affect mass measurements involving electrons, such as the B^+ mass measurements in the $B^+ \rightarrow \mu^+ \nu_\mu e^+ e^-$ decay, they do not alter the E/pc ratio used for electron identification. To enhance momentum reconstruction, a dedicated Bremsstrahlung recovery technique is employed. Photon candidates, represented by neutral clusters with transverse energy exceeding 75 MeV and located within a defined region of the ECAL, extrapolated from the electron track upstream of the magnet, are included in the measured electron momentum.

Hadronic calorimeter: The HCAL is an iron-based sample calorimeter with scintillating tiles acting as the active and absorbent material. Its primary function is to identify hadrons and produce energy measurements. The thickness of the hadrons is taken at 5.6 interaction length and its resolution is given by the equation:

$$\frac{\sigma_E}{E} = \frac{(69 \pm 5)\%}{\sqrt{E}} \oplus (9 \pm 2)\% \quad (4.3)$$

for the energy given in GeV.

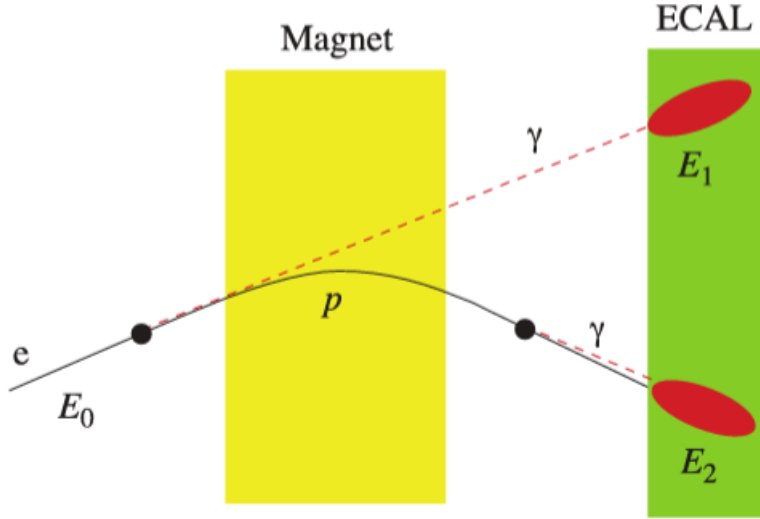


Figure 4.12: Schematic representation of Bremsstrahlung photons emitted by an electron before and after the magnet. Figure taken from [30].

Muon system

Muons are often found in the final states of b decays, like the decays studied in this work, hence a sophisticated system for muon detection is needed. In LHCb, there are five muon stations named M1-5 in the order of their position from the interaction point respectively (Fig. 4.3). They provide efficient muon triggering, as well as tracking and particle identification.

M1 is located upstream of the calorimetry system, to improve the transverse momentum (p_T) in the trigger. M2-5 are placed downstream of the calorimetry systems. In the muon stations, Multi Wire Proportional Chambers technology is used. Between the stations, 80 cm thick iron absorbers have been placed to minimize the hadronic background. In the special case of the M1 the inner region of the station is made out of gas electron multipliers (GEMs), to adjust the high flux of particles passing through it. Figure 4.13 is a representation of the muon system.

The minimum energy for a muon to pass through all of these stations is approximately 6 GeV. The M1-3 stations have a high spatial resolution on the x-axis, so they can define the track direction and a transverse momentum p_T resolution of the order of 20%. The M4-5 stations have lower resolution, however, their aim is mainly to identify highly penetrating muons [25]. The muon stations have an acceptance of 20-306 mrad for the bending and 16-258 mrad for the non-bending planes respectively. The muon selection efficiency in the $0.8 < p_T < 1.7$ GeV region is larger than 92% and for $p_T > 1.7$ GeV larger than 96%. The misidentification rate of muons with protons, pions, and kaons is of the order of 1-2% for the latter rate [7, 9].

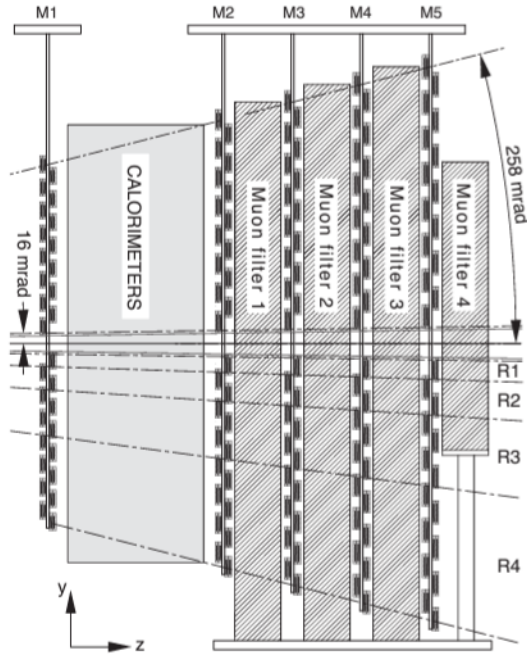


Figure 4.13: Side view of the muon system. Figure from [7]

4.2.4 Trigger

An important part of the LHCb apparatus is also the triggering system. The trigger selects all data used for future analysis, and thus having an understanding of its functions gives one a greater insight into the processing of primary data. The LHCb trigger system can be segregated into two subsystems, the low-level pure hardware part Level zero (L0) and the High-Level Triggers (HLT1 and HLT2) implemented in software. Figure 4.14 is an illustration of the triggering process during Run2 in LHCb. Further details of the LHCb triggers can be found in [31].

L0 trigger

The L0 trigger is implemented on hardware and pulls useful information from the calorimeters and the muon stations. It aims to reduce the 40MHz bunch-crossing rate to 1 MHz, a value that the detector is capable to read out. Because this process must be done in an extremely small time window, less than $4\mu\text{s}$, the L0 has strict threshold criteria taken directly from the calorimeters and the muon stations, as stated above. In Table 4.1 one can see the different L0 thresholds.

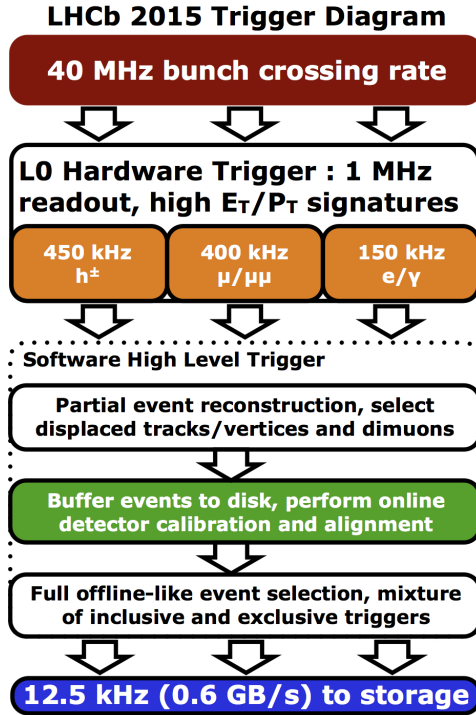


Figure 4.14: Illustration of the triggering process in LHCb during Run2 (year: 2015). Figure from [32].

Table 4.1: Summary of the different L0 thresholds in Run2. All numbers were taken from [33].

L0 Trigger	E_T/p_T threshold			SPD threshold
	2015	2016	2017	
Hadron	$> 3.6 \text{ GeV}$	$> 3.7 \text{ GeV}$	$> 3.46 \text{ GeV}$	< 450
Photon	$> 2.7 \text{ GeV}$	$> 27.8 \text{ GeV}$	$> 2.47 \text{ GeV}$	< 450
Electron	$> 2.7 \text{ GeV}$	$> 2.4 \text{ GeV}$	$> 2.11 \text{ GeV}$	< 450
Muon	$> 2.8 \text{ GeV}$	$> 1.8 \text{ GeV}$	$> 1.35 \text{ GeV}$	< 450
Muon high p_T	$> 6.0 \text{ GeV}$	$> 6.0 \text{ GeV}$	$> 6.0 \text{ GeV}$	–
Dimuon	$> 1.69 \text{ GeV}^2$	$> 2.25 \text{ GeV}^2$	$> 1.69 \text{ GeV}^2$	< 900

HLT

L0-accepted events are moved to an event filter farm, consisting of a series of computers so that the reconstruction and selection can take place. On each processor in the farm, the Event Filter uses a C++ executable that selects and reconstructs events similarly to the offline processing stage. The amount of time that may be used to reconstruct a single event, however, is the primary distinction between online and offline selection. The maximum time for online reconstruction is often about 50ms, but offline reconstruction requires roughly 2s per event.

The HLT trigger is made up of several trigger options, each of which is intended to gather a particular set of events depending on the kinematic characteristics of charged and neutral particles, the decay topology, and the particle identities. Individual trigger choices can be prescaled if the accepted event rate is too high by randomly choosing just the events that meet their requirements. At HLT1, tracks are reconstructed only in the VELO and selected based on their probability to come from heavy flavor decays. At HLT2, complete forward tracking of all tracks reconstructed in the VELO and also of tracks reconstructed only outside of the VELO is performed. Several trigger selections, either inclusive or exclusive, are available at this stage.

HLT1 and HLT2 each receive a portion of the overall HLT processing time. The intricacy of the information that each HLT is capable of processing and the amount of time they have to do so, are the key distinctions between HLT1 and HLT2. The acceptable event rate is partially reconstructed in the first step to bring it down to 30 kHz, and a more thorough reconstruction is performed in the second stage.

Chapter 5

Monte Carlo Simulation

This chapter presents the Monte Carlo simulation used in this analysis [34, 35].

5.1 Effective Hamiltonian

The effective Hamiltonian in the decay of study can be expressed as:

$$\mathcal{H}_{eff}(x) = \mathcal{H}_{weak}(x) + \mathcal{H}_{EM}(x) \quad (5.1)$$

for both interactions to contribute to it. The weak Hamiltonian is given as:

$$\mathcal{H}_{weak}(x) = -\frac{G_F}{\sqrt{2}} V_{ub} (\bar{u}(x) \gamma^\mu (1 - \gamma^5) b(x)) (\bar{\mu} \gamma_\mu (1 - \gamma^5) \nu_\mu(x) + h.c.), \quad (5.2)$$

while the electromagnetic component is given as:

$$\mathcal{H}_{EM} = -e \sum Q_f (\bar{f}(x) \gamma^\mu f(x)) A_\mu(x) = -j_{EM}^\mu A_\mu(x), \quad (5.3)$$

with Q_f , the charge of the fermion of the flavor f in units of the unitary charge, $f(x)$, the fermionic field of flavor f , for which $u(x)$, $b(x)$, $\mu(x)$, $e_-(x)$, $e_+(x)$ and $\nu_\mu(x)$ the quark, and leptons respectively, and $A_\mu(x)$, the four-potential of the electromagnetic field ¹⁹.

¹⁹All normalisations and variables are defined as in [2].

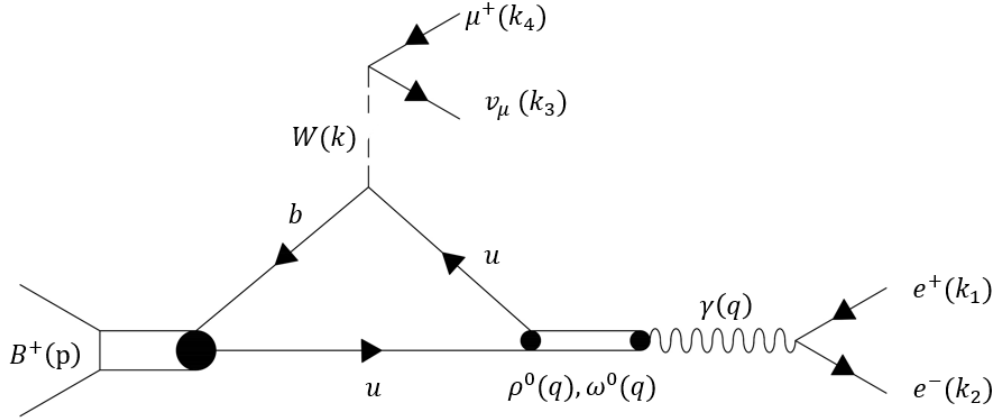


Figure 5.1: Virtual-photon emitted from the light quark of the B meson. Figure taken from [34]

5.2 Matrix elements

The total matrix element in accordance with the \mathcal{H}_{eff} is given as an addition to the three individual contributions explained in detail below.

$$M_{fi} = M_{fi}^{(u)} + M_{fi}^{(b)} + M_{fi}^{(\ell)} \quad (5.4)$$

5.2.1 Virtual photon emission from the u quark of the B meson

The first term in 5.4 corresponds to the virtual photon emission from the B meson's u-quark. In this instance, the virtual photon contribution is represented by the vector meson dominance model (VMD), which includes intermediate resonances, as depicted in Figure 5.1.

The matrix element of the B^+ decay here is given as:

$$M_{fi}^{(u)} = \frac{G_F}{\sqrt{2}} 4\pi\alpha_{EM} V_{ub} \frac{1}{q^2} \sum_{i=\rho^0, \omega} \frac{f_V^i M_i I_i}{q^2 - M_i^2 + i\Gamma_i M_i} F_{\mu\nu}^{(i)}(k^2) (\bar{e}_-(k_2) \gamma^\nu e_+(k_1)) (\bar{\nu}(k_3) \gamma_\mu (1-\gamma^5) \mu(k_4)). \quad (5.5)$$

Here, only the ρ^0 and ω resonances are taken as contributions, by the coefficient I_i .

5.2.2 Virtual photon emission from b quark of the B meson

Virtual photon emission from the heavy quark of B meson is illustrated in Figure 5.2. Here, a middle-weight vector meson B^{*+} decays to a virtual photon and an intermediate pseudoscalar meson B^+ . This contribution is small but contributes visibly because of interference with the other diagrams.

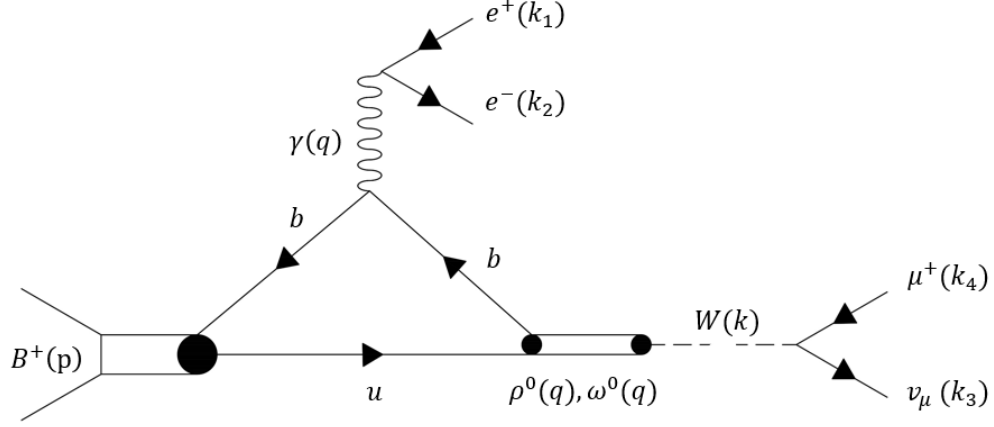


Figure 5.2: Virtual-photon emitted from the heavy quark of the B -meson. Figure taken from [34].

The Matrix element here is given as:

$$M_{fi}^{(b)} = \frac{2 G_F}{3 \sqrt{2}} 4\pi\alpha_{EM} V_{ub} \frac{1}{q^2} \frac{M_{B^*} f_{B^*}}{k^2 - M_{B^*}^2} \frac{V_b(q^2)}{M_1 + M_{B^*}} \epsilon_{\mu\nu\rho\sigma} (e^-(k_2) \gamma^\nu e^+(k_1)) (\bar{\nu}(k_3) \gamma^\mu (1 - \gamma^5) \mu(k_4)) \quad (5.6)$$

5.2.3 Virtual photon emission from the lepton in final state

The final diagram contributing to the amplitude describes the photon released by the lepton in its final condition. The photon pole on the q^2 -variable and lepton masses in their final state here could not be deduced as in the other cases. Figure 5.3 represents this case. The matrix element of the B^+ can be written as follows:

$$M_{fi}^{(\ell)} = \frac{G_F}{\sqrt{2}} 4\pi\alpha_{EM} V_{ub} \frac{f_{B_u}}{q^2} g_{\mu\nu} (e^-(k_2) \gamma^\nu e^+(k_1)) (\bar{\nu}(k_3) \gamma^\mu (1 - \gamma^5) \mu(k_4)) \quad (5.7)$$

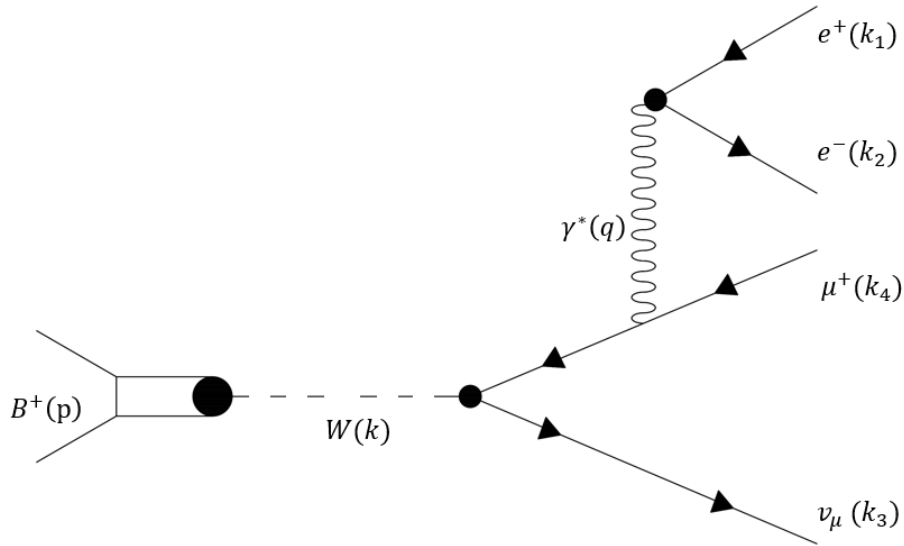


Figure 5.3: Virtual-photon emitted from the lepton in the final state. Figure taken from [34].

5.3 Monte Carlo parametrisation

Using the above calculations, the kinematics of the $B^+ \rightarrow \mu^+ \nu_\mu e^+ e^-$ decay is simulated. The parameters defining the kinematics of the decay are:

1. The q^2 , defined as the dielectron mass
2. The k^2 , defined as the invariant mass of the neutrino and the muon
3. The angle θ_γ , defined as the angle between the direction of the B^+ and the direction of one of the electrons, in the dielectron's rest-frame (q^2 -plane)
4. The angle θ_W , defined as the angle between the direction of the B^+ and the direction of the muon, in the muon-neutrino's rest-frame (k^2 -plane)
5. The angle ϕ , defined as the angle between the q^2 and k^2 planes in the rest-frame of the B^+ .

Though the Monte Carlo from [34] has limitations, these limitations mainly apply at the low q^2 region when transformed for electrons. Since the selection of events, is however done on the ρ^0 resonance²⁰ this is not an issue for the analysis. This model is cross-checked by comparing the simulation model with results from [36].

²⁰As explained in detail in Subsection 8.1.1, the m_{ee} selection is made in the [600,1000] MeV range.

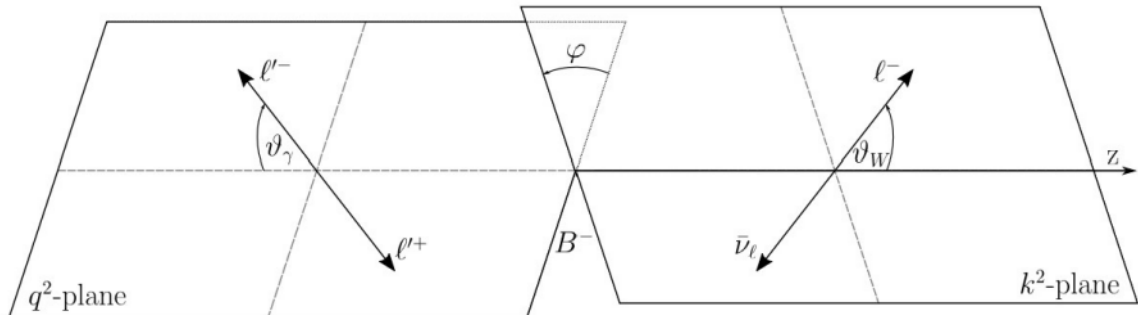


Figure 5.4: Graphical representation of the θ_γ , θ_W and ϕ angles, where the denotion ℓ stands for muons and the denotion ℓ' stands for electrons. Figure provided by Fabian Glaser.

5.4 Development of the Monte Carlo

Using the model described above the MC simulation for the $B^+ \rightarrow \mu^+ \nu_\mu e^+ e^-$ is developed. The simulation statistically generates data that are intended to behave like experimental data. To generate the events two main packages are being used, namely GAUSS [37] and BOOLE [38]. The use of these two packages ensures that the simulated data undergo the same process as the experimentally collected data do.

The GAUSS framework estimates physics simulations and coordinates multiple external applications. A special LHCb configuration generates pp event collisions through PYTHIA8 [39]. EvtGen [40] is used to simulate the decay amplitudes of the different hadronic particles, with the use of the information gathered from DecFiles [41] about their various decay channels and branching ratios (\mathcal{BR}). From there PHOTOS [42] provides the final state radiation, while Geant4 [43] simulates every particle's interaction with the detector and provides the hits for every subdetector. Before the Geant4 step, additional cuts can be added to apply more generator-level restrictions to the simulated data.

The Gaudi framework, on which BOOLE is based on, offers facilities for sequencing algorithms. Here the response of the various subdetectors and electronics is imitated. BOOLE aims to convert the MC hits into an electronic signal and implement the L0 trigger. Here, one must point out that aspects of the L0 are often simulated with low accuracy, mainly due to L0 being a hardware trigger.

All later steps of data processing are the exact same for both MC and experimental data.

Chapter 6

Analysis strategy

This chapter summarizes the strategy followed for calculating the number of reconstructed $B^+ \rightarrow \mu^+ \nu_\mu e^+ e^-$ events in 2016-18 Run2 LHCb data.

6.1 Signal estimation technique

The ultimate objective of the analysis is to measure the branching ratio of the $B^+ \rightarrow \mu^+ \nu_\mu e^+ e^-$ decay. In order to achieve this goal, a measurement of the number of reconstructed $B^+ \rightarrow \mu^+ \nu_\mu e^+ e^-$ events is correlated with its branching ratio, using the total efficiencies and the reference channel's $B^+ \rightarrow K^+ J/\psi(e^+ e^-)$ measurements.

At this stage of the analysis, the goal is to estimate how many signal events can be expected in the data set for the branching ratio prediction provided by theorists [36]. The formulae presented in this section, are used in the context of this thesis, with the branching ratio of the $B^+ \rightarrow \mu^+ \nu_\mu e^+ e^-$ decay as an input, to get an estimate of the expected number of events in the LHCb Run2 2016-18 data set.

In order to estimate the number of reconstructed $B^+ \rightarrow \mu^+ \nu_\mu e^+ e^-$ events in 2016-18 Run2 LHCb data, a study relative to the reference channel $B^+ \rightarrow K^+ J/\psi(e^+ e^-)$ is conducted. The number of reconstructed events is given by the equation:

$$N_f = \mathcal{L}_{LHCb} \cdot \sigma_{b\bar{b}} \cdot 2f_u \cdot \mathcal{BR}(B^+ \rightarrow f) \cdot \epsilon_{tot}(f), \quad (6.1)$$

where N_f represents the number of events, \mathcal{L}_{LHCb} represents the integrated luminosity of the LHCb experiment, which is a measure of the total number of particle collisions that have occurred during a specific time period, $\sigma_{b\bar{b}}$ represents the cross section of a $b\bar{b}$ pair in the LHC, which is a measure of the likelihood of a $b\bar{b}$ pair being produced in the accelerator, $2f_u$, the fragmentation fraction for forming a B^+ multiplied with a factor two, to adjust for hadronization of both b and \bar{b} , $\mathcal{BR}(B^+ \rightarrow f)$ denotes the branching ratio, which represents the probability of the specific decay or particle process leading to the desired final state, and $\epsilon_{tot}(f)$ denotes the detector efficiency, which is the probability of a signal event being detected and recorded by the detector. Here the index f stands for the final state.

There are, however, effects that cause a large uncertainty, when implementing this direct approach. For starters, there is a large uncertainty on the $\sigma_{b\bar{b}}$. The source of this uncertainty is the difficulty to measure the cross section in the production spectrum of the $b\bar{b}$, within the LHCb experiment. This is in part due to the experiment's geometry, which does not have a 4π angular acceptance in the azimuthal coordinate, as well as statistical limitations, and systematic effects on the cross-section measurement. In addition, the systematic uncertainty related to the absolute efficiency which is obtained from the M simulation, makes such a direct calculation have a larger uncertainty. The various systematic efficiencies in selecting, reconstructing, and measuring the various physical quantities necessary contribute to the unclear picture and motivate further the need for another method to estimate the number of reconstructed $B^+ \rightarrow \mu^+\nu_\mu e^+e^-$ events more accurately. For all these reasons, a relative to a reference channel study is used to estimate the expected number of reconstructed $B^+ \rightarrow \mu^+\nu_\mu e^+e^-$ events.

The chosen reference channel for this work is the $B^+ \rightarrow K^+J/\psi(e^+e^-)$ decay. B^+ mesons are produced copiously by the LHC accelerator, with many of them decaying through this channel because of its large branching ratio²¹. This decay has an electron-positron pair in its final state, just like the target decay. Additionally, it doesn't have a neutrino in the final state, which results in a better resolution.

This method, utilizing the reference channel, determines the expected number of signal events as follows:

$$N_{\mu\nu ee} = N_{Kee} \cdot \frac{\mathcal{BR}(B^+ \rightarrow \mu^+\nu_\mu e^+e^-)}{\mathcal{BR}(B^+ \rightarrow K^+J/\psi) \cdot \mathcal{BR}(J/\psi \rightarrow e^+e^-)} \cdot \frac{\epsilon_{\text{tot}(B^+ \rightarrow \mu^+\nu_\mu e^+e^-)}}{\epsilon_{\text{tot}(B^+ \rightarrow K^+J/\psi(e^+e^-))}}, \quad (6.2)$$

where $N_{\mu\nu ee}$ and N_{Kee} represents the number of events for each decay in data, and $\epsilon_{\text{tot}(B^+ \rightarrow \mu^+\nu_\mu e^+e^-)}$ and $\epsilon_{\text{tot}(B^+ \rightarrow K^+J/\psi(e^+e^-))}$ the total efficiencies for each decay channel, given as:

$$\epsilon_{\text{tot}} = \epsilon_{\text{selection}} \cdot \epsilon_{\text{generator}}, \quad (6.3)$$

where:

$$\epsilon_{\text{selection}} = \frac{N_{\text{SelectedEventsInSimulation}}}{N_{\text{AllEventsInSimulation}}}, \quad (6.4)$$

and $\epsilon_{\text{generator}}$ the efficiency given by the MC simulation.

Using equation 6.2 has the benefit of canceling out some of the uncertainties found in equation 6.1, such as the uncertainties stemming from the integrated luminosity of the LHCb measurement and the $\sigma_{b\bar{b}} \cdot 2f_u$ product. Additionally, systematic uncertainties of features exhibited in both channels also cancel, like on the measurements of the B^+ flight direction in the detector, the reconstruction of the dielectron object measurements, or the reconstruction of the B^+ to three tracks with two electrons.

Although this method (Eq. 6.2) produces more precise results than the direct method

²¹For comparison, the reference channel branching ratio is more than an order of magnitude larger than the branching ratio of the signal.

described by equation 6.1, there are still limitations on its resolution. An important limitation originates in the existence of a kaon instead of a muon in the reference channel. In the signal channel, the muon is used for triggering at the L0 level, which cannot be done in the reference channel. Moreover, the reference channel has a larger reconstruction efficiency than the signal channel, due to the lack of a neutrino in the final state. Last but not least, the reference channel selects data with the dielectron mass around the J/ψ ($m_{J/\psi} \approx 3096\text{MeV}$), while the selection of signal data is done around the ρ^0 resonance ($m_\rho \approx 770\text{MeV}$)²². This can have an impact on the selection efficiency, due to it being strongly correlated with the p_T of the dielectron object. This means that the electron-positron pair might not have sufficient p_T to pass the selection threshold.

6.2 Corrected mass

To connect the final state $\mu^+\nu_\mu e^+e^-$ recorded in the detector, as originating from the B^+ , the invariant mass of the final state must be equal to the invariant mass of the B^+ . However, as explained in Section 3.1, the neutrino is invisible to the detector. This means, that the reconstructed invariant mass is always less than the true invariant mass of the B^+ .

To mitigate this issue, one can parametrize the expected value of the momentum carried by the neutrino, by finding the so-called corrected mass. The corrected mass is given by the equation [44]:

$$M_{\text{corr}} = \sqrt{M_{\mu ee}^2 + |p_\perp|^2 + |p_\perp|}, \quad (6.5)$$

where M_{corr} is the corrected mass of the B^+ , $M_{\mu ee}$ the visible mass recorded in the detector, and p_\perp the visible momentum is perpendicular to the flight direction of the B^+ ²³. The M_{corr} by its nature is however only a lower estimate, i.e. it underestimates the true invariant mass of the B^+ . In Figure 6.1 a comparison of the M_{corr} and $M_{\mu ee}$ is presented.

For this thesis, all measurements concerning the mass of the B^+ meson in the $B^+ \rightarrow \mu^+\nu_\mu e^+e^-$ decay are performed with the M_{corr} .

²²As explained in detail in Subsection 8.1.1.

²³The flight direction of the B^+ is determined by using the PV and SV.

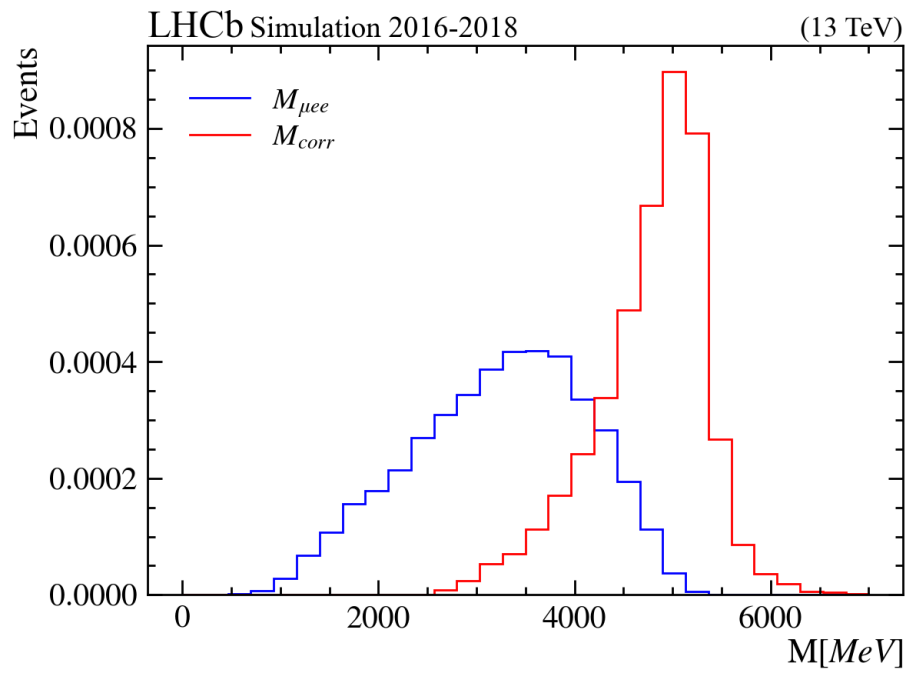


Figure 6.1: Comparison of the M_{corr} and $M_{\mu ee}$

Chapter 7

Data processing

As stated in the introduction, the aim of this work is to estimate the number of $B^+ \rightarrow \mu^+ \nu_\mu e^+ e^-$ events in the data collected in 2016-18. This chapter describes the necessary steps, in order to select the data required for the analysis process. This selection can be split into three steps, online selection, stripping, and preselection.

7.1 Online selection

The online selection consists of the trigger systems, as described in Subsection 4.2.4. Each trigger imposes different cuts, on the data, which are then also applied in the Monte Carlo²⁴ sample used for the analysis.

The initial stage is to opt for a trigger setup that can isolate the signal. This means, that at the L0 level, the triggering is not necessarily on a specific signal, but on the presence of particles like the ones in the signal being investigated. After an overall L0 selection, a targeted collection of HLT lines is formed to single out events according to the signal's kinematics and topology. Only the events that exhibit features that match the signal candidate are allowed to pass through the trigger selection. These selected events are known as TOS events, which stands for Trigger On Signal. This procedure makes it easier to replicate the trigger response in simulations.

For the L0 trigger, the L0Muon and L0Electron trigger lines are used. These requirements trigger on the particles of the signal decay. The L0 trigger of the signal channel efficiency is estimated to be of the order of 21.1%²⁵.

At the HLT1 trigger level, the Hlt1TrackMVA, HltTwoTrackMVA, and Hlt1TrackMuon trigger lines have been chosen. Their combined efficiencies estimates are calculated to be 97.5%²⁶. Finally, the Hlt2Topo[2,3]Body and Hlt2TopoMu[2,3]Body trigger lines are taken for HLT2,

²⁴the nSND cut of the L0 trigger cannot be well reproduced in the Monte Carlo data. Relevant adjustments have been done to mitigate this effect.

²⁵These numbers were provided by Fabian Glaser.

²⁶These numbers were provided by Fabian Glaser.

with an estimated efficiency of 90.0%²⁷.

7.2 Data stripping

After the online selection requirements are implemented, the next step is the data-stripping process. The stripping data processing is done offline, but it is very demanding in terms of computing resources and therefore it is performed centrally by the LHCb collaboration. The process involves a series of stripping lines that enhance the conditions set by the trigger lines. The key contrast is that stripping draws on information from the complete event reconstruction, allowing for a more targeted signal selection. For this work, the B23MuNu_Muec stripping line is used.

In this study, the decay of B^+ particles is examined by reconstructing them using three charged tracks. The tracks selected must meet certain criteria: they should be of good quality, not originating from any primary vertex (PV), identified as a muon and two electrons, and form a secondary vertex (SV) that is well displaced from any PV. To determine the associated primary vertex, the concept of χ_{IP}^2 is utilized, which compares the vertex-fit χ^2 of a PV reconstructed with and without including the B^+ trajectory. Additionally, it is required that the momentum vectors of the B^+ decay products align with the line connecting the associated PV and the SV, accounting for the momentum carried by the neutrino involved in the decay.

7.2.1 Bremsstrahlung in the dielectron pair

As explained in Subsection 4.2.3, when analyzing events with electrons, it is important to account for Bremsstrahlung radiation. In the $B^+ \rightarrow \mu^+ \nu_\mu e^+ e^-$ decay analysis, this plays an even greater role, since two electrons are present in the final state. In signals like the $B^+ \rightarrow \mu^+ \nu_\mu e^+ e^-$, that have small m_{ee} values, double counting of Bremsstrahlung photons can occur. This is because the assignment of Bremsstrahlung, as it is introduced in Subsection 4.2.3, is done separately for each individual electron track. Consequently, in events with small m_{ee} values and by extension small opening angles, the same neutral cluster is attributed as Bremsstrahlung to both electron candidates.

Such an effect was not taken into account initially from the stripping line. As a result, the first MC studies, without the adjustment for double counting of the Bremsstrahlung, show an excess of the signal at the right tail of the distribution of the M_{corr} for events with more than one Bremsstrahlung photon. This can be seen in Fig. 7.1, where the M_{corr} of events with zero, one, and more than one Bremsstrahlung photons is plotted.

To mitigate this issue, the DiElectronMaker is used after the stripping process. The DiElectronMaker solves the double-counting issue, by ignoring the previous Bremsstrahlung assignment and doing it again. However, instead of repeating the process again on individual tracks as in Subsection 4.2.3, it takes into account both tracks simultaneously and

²⁷These numbers were provided by Fabian Glaser.

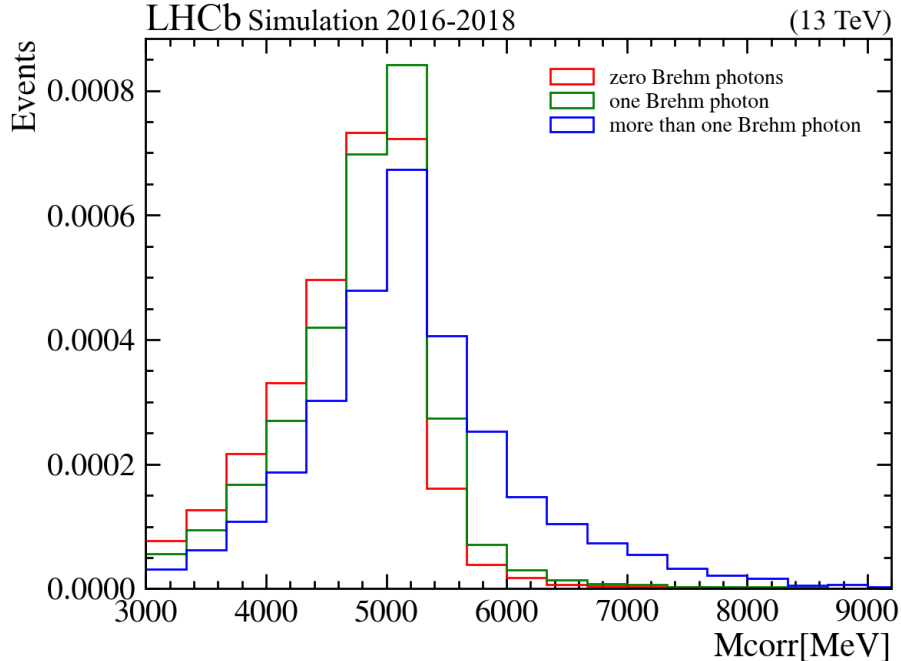


Figure 7.1: Distribution of the M_{corr} for events with zero, one, and more than one Bremsstrahlung photons.

whenever a Bremsstrahlung photon is compatible with both electrons, it attributes its energy randomly to one of the two to avoid double counting. The MC simulation used in this study shows a clear improvement in the M_{corr} resolution when using this approach. The standard stripping along with the stripping after the application of the DiElectronMaker is plotted in Fig. 7.2. Figure 7.3 illustrates the variation in the number of Bremsstrahlung photons attributed to an event after the application of the DiElectronMaker.

7.3 Preselection

The final step of the selection process is the offline selection. The offline selection imposes extra cuts and filters on the collected data. These constraints can be measured quantities, like the invariant mass of the detected particles of an event, limits in the kinematic region, or indices representing some detector response²⁸. Such criteria belong in the preselection cuts of the analysis.

On the B^+ three main categories of cuts are applied. The DIRA cut makes sure that the PV-SV-axis is aligned with the momentum of the B^+ . The χ^2_{FD} cut ensures the position separation of the PV and the SV, while also loose general mass cuts are applied around the region of study. On the dielectron object a χ^2_{IP} cut is implemented, similar to the one in the stripping, on the SV of the decay. Additionally, the di-electron χ^2_{FD} and di-electron FD cuts

²⁸for example the ProbnNe index

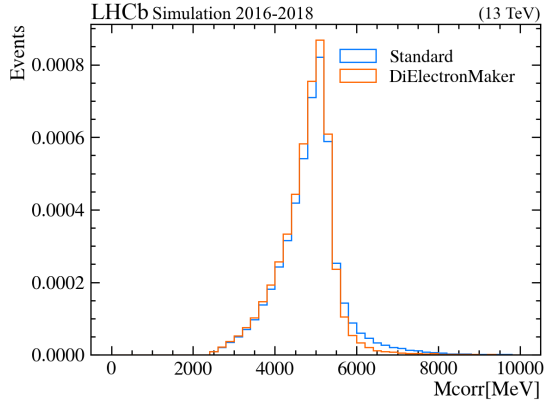


Figure 7.2: Comparison of $B^+ \rightarrow \mu^+ \nu_\mu e^+ e^-$ candidates in simulation with and without running DiElectronMaker in the production of n Tuples.

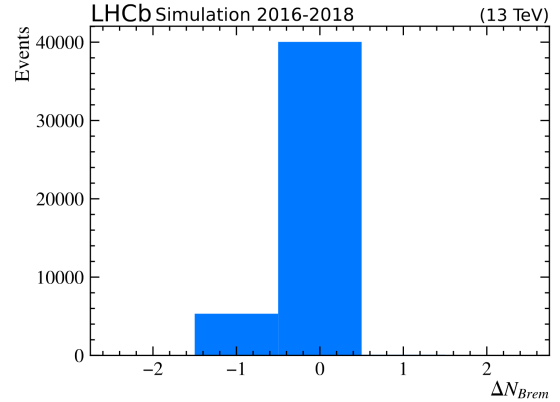


Figure 7.3: Variation in the number of Bremsstrahlung photons attributed to an event after the application of the DElectronMaker.

are applied to the data, to guarantee that the dielectron object does not fly in the detector, while the e^\pm VeloCharge cut ensures that the electrons do not originate from a photon conversion. The electrons and muons have selection criteria based on the hits and associated cluster hits of the detector. Finally, cuts are applied on the distance of closest approach (DOCA), which indicates a common origin of tracks, and on the opening angle between the muon and an electron (OA), which ensures that there is no track overlap. A summary of the preselection criteria used for this work can be found in Table 7.1. It is noteworthy, that some of the criteria in the offline selection exist also in the stripping, however, the offline adjustments are stricter.

To mitigate backgrounds in the data sets, vetoes have been also set. Peaks of the K^{*0} and D^0 resonances are expected in the m_{ee} spectrum. To suppress this type of double misID background, the use of the veto filters described in Table 7.2 is needed. In this study, the veto strategy involves identifying cases where hadrons are misidentified as the electrons, as in the case of $K \rightarrow e$ and $\pi \rightarrow e$ misID, in $B^+ \rightarrow D^0 \mu^+ \nu$ decay mode. Additionally, the aim is to veto the $B^+ \rightarrow D^0 e^+ \nu$ decay mode, where one hadron is misidentified as a muon and the other as an electron, as in the case of $K \rightarrow \mu$ and $\pi \rightarrow e$ ²⁹.

²⁹These cuts were taken from [45] and implemented by Fabian Glaser.

Table 7.1: Summary of the preselection criteria for the $B^+ \rightarrow \mu^+ \nu_\mu e^+ e^-$ decay.

B^+	DIRA > 0.995 $\chi_{FD}^2 > 100$ $500 \text{ MeV} < m_{visible(\mu^+ e^+ e^-)} < 6000 \text{ MeV}$ $-5 \text{ GeV}^2 < m_{miss}^2 < 10 \text{ GeV}^2$
$e^+ e^-$	$\chi_{IP}^2 > 40$ di-electron $\chi_{FD}^2 < 9$ di-electron FD < 20 $e^\pm \text{ VeloCharge} < 1.25$
e^\pm	hasCalo, hasRich, inAccEcal L0Calo_ECICAL_region ≥ 0 abs(L0Calo_ECICAL_xProjection > 363.6) OR abs(L0Calo_ECICAL_yProjection > 282.6) $p_T > 300 \text{ MeV}, p_{T,track} > 200 \text{ MeV}$ PIDE > 2.0, PIDE - PIDK > 0.0, ProbNNe > 0.2
μ^+	hasCalo, hasMuon, isMuon $p_T > 1200 \text{ MeV}$ PIDmu > 0.0, PIDmu - PIDK > 0.0, ProbNNmu > 0.2
other	$\max \chi_{DOCA}^2(\mu^\pm, e^+, e^-) < 9$
Clone	OA(e^\pm, μ^+) > 0.005

Table 7.2: Vetoes placed on the $B^+ \rightarrow \mu^+ \nu_\mu e^+ e^-$ decay data.

$B^+ \rightarrow \mu^+ \nu D^0(K^+ \pi^-)$	$e^+ \text{ProbNN}K > 0.4, e^- \text{ProbNN}pi > 0.4$ $ m_{ee \rightarrow K\pi} - m_{D^0} < 30 \text{ MeV}$
$B^+ \rightarrow \mu^+ \nu D^0(\pi^+ \pi^-)$	$e^\pm \text{ProbNN}pi > 0.4$ $ m_{ee \rightarrow \pi\pi} - m_{D^0} < 30 \text{ MeV}$
$B^+ \rightarrow \mu^+ X K^{*0}(K^+ \pi^-)$	$e^+ \text{ProbNN}k > 0.4, e^- \text{ProbNN}pi > 0.4$ $ m_{ee \rightarrow K\pi} - m_{K^{*0}} < 50 \text{ MeV}$

Chapter 8

Analysis

This chapter presents a summary of the calculated results for the expected number of $B^+ \rightarrow \mu^+ \nu_\mu e^+ e^-$ events using the 2016-18 Run2 LHCb data.

8.1 Signal channel

To ensure the quality and reliability of the analysis, selection cuts are applied on the dielectron mass in the [600,1000] MeV range and the mass of the B^+ meson in the [4000,6000] MeV range. The section presents these selection criteria and the effects they have on signal resolution.

8.1.1 Dielectron mass

In Section 3.2, where the $B^+ \rightarrow \mu^+ \nu_\mu e^+ e^-$ decay is introduced, different resonances of the photon spectrum are mentioned. For the purpose of this study, these intermediate resonances can be useful. Since the number of virtual photons drops exponentially with respect to their invariant mass, the number of events of high q^2 in the detector drop. Thus, the selection of counts with higher m_{ee} is going to be more difficult.

The $B^+ \rightarrow \mu^+ \nu_\mu \pi^0$ with $\pi^0 \rightarrow e^+ e^- \gamma$ and $B^+ \rightarrow \mu^+ \nu_\mu \eta$ with $\eta \rightarrow e^+ e^- \gamma$ decays are also important backgrounds to the signal decays, which have to be filtered out effectively. As shown in Figure 8.1 the $\pi^0 \rightarrow e^+ e^- \gamma$ and $\eta \rightarrow e^+ e^- \gamma$ modes do have contributions in the range of interest around the B^+ meson mass. Furthermore, the emission of Bremsstrahlung from the electrons can also play a negative role in the resolution.

In order to mitigate these effects without removing much signal, the selection of the $B^+ \rightarrow \mu^+ \nu_\mu e^+ e^-$ decays is done with the prerequisite, that the m_{ee} is on the ρ resonance, specifically in the [600,1000] MeV range. This choice has the role of firstly suppressing any systematic uncertainties, due to the ρ being a well-defined resonance, and reducing the π^0 and η backgrounds. The cut does not allow for m_{ee} to exceed 1 GeV since significant signal contributions are not expected in this region and theoretical predictions are not available there [35]. Figure 8.2 is a graphical representation of the m_{ee} selection. Along with the signal mode, the π^0

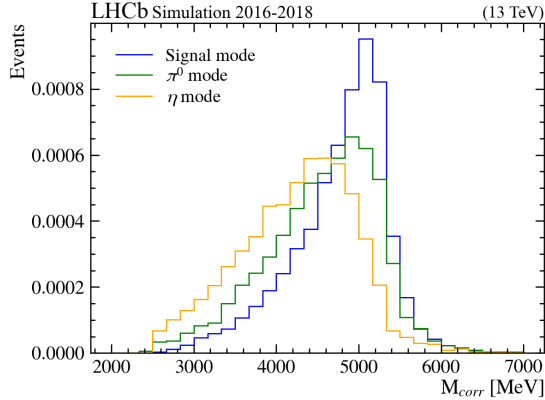


Figure 8.1: M_{corr} distribution of the signal, π^0 and η modes.

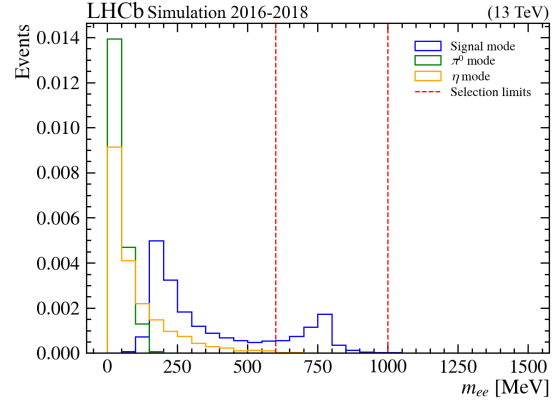


Figure 8.2: m_{ee} distribution of the signal, π^0 and η modes.

and η background modes are plotted. Noteworthy to point out in Fig 8.2 is that the cut of the m_{ee} at around 100 MeV in the signal mode is not due to a physical effect, but because of a threshold on the MC simulation.

8.1.2 B^+ mass calculation

To establish a connection between the final state $\mu^+\nu_\mu e^+e^-$ recorded in the detector and the B^+ , the invariant mass of the final state must be equal to the invariant mass of the B^+ . As explained in 6.2, because the neutrino is untraceable by the detector the M_{corr} variable is measured instead. The simulation contains all intermediate resonances, but only candidates with m_{ee} in the range of the ρ mass [600,1000] are selected. After applying the cut on m_{ee} the M_{corr} cut follows. The acceptance region for the signal is set to the [4000,6000] MeV range. Figure 8.3 represents the acceptance window for the $B^+ \rightarrow \mu^+\nu_\mu e^+e^-$ decays.

Uncertainties of the M_{corr} measurement

One can observe a tail at the lower range of the M_{corr} distribution depicted in Fig. 8.3. This feature exists, in part due to the corrected mass being by definition an approximation of the true mass of the B^+ . This is demonstrated by Fig. 8.4.

In the M_{corr} there are two main sources of uncertainty in the measurement, the momentum reconstruction of the e^\pm and μ , and the direction reconstruction of the B^+ . In Figure 8.4 the effects of these two uncertainties are compared, by plotting them along with the true corrected mass of the B^+ ³⁰. These two effects have a comparable full-width-half-maximum. The uncertainty of the momentum tends to underestimate the M_{corr} . This is to be expected since the electrons emit Bremsstrahlung and the Bremsstrahlung recovery algorithm has a limited efficiency. This causes often the detector to underestimate the electron energy because of the emitted Bremsstrahlung photon. On the other hand, the uncertainty of the

³⁰As true are defined the values for different variables generated by the MC simulation, before them being passed through the detector.

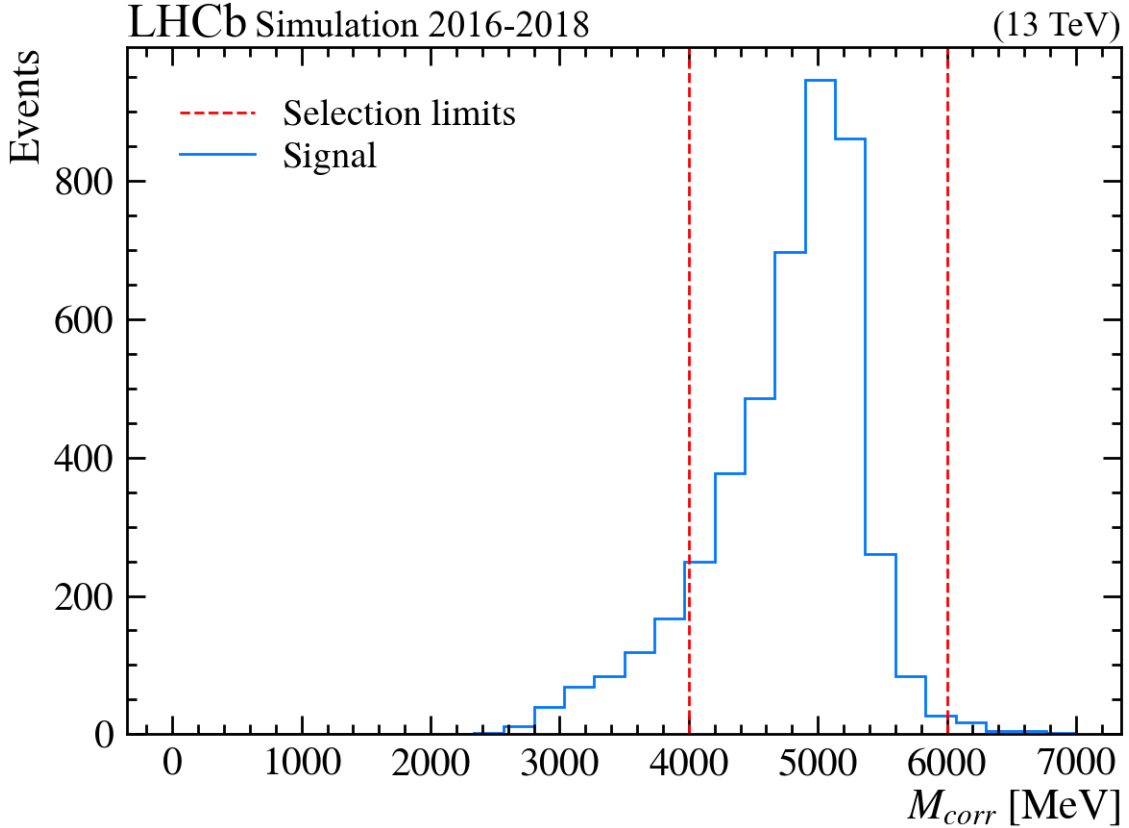


Figure 8.3: Corrected mass of the B^+ meson, of the $B^+ \rightarrow \mu^+ \nu_\mu e^+ e^-$ decay in simulation.

direction is more symmetrical. This symmetry arises from the statistical nature of the detection process, where the spatial resolution is determined by factors such as the detector's granularity, the spatial resolution of sensors, and the number of detected hits. The shapes of the uncertainties can be also seen in Fig. 8.5, where the difference between the reconstructed values of M_{corr} and the true values of M_{corr} are presented.

Finally, a tail also towards the lower range of the M_{corr} distribution of all three cases, i.e. reconstructed momentum, reconstructed direction, and true values, depicted in Figure 8.4 shows, that the source of the tail is in large part because of the M_{corr} function itself.

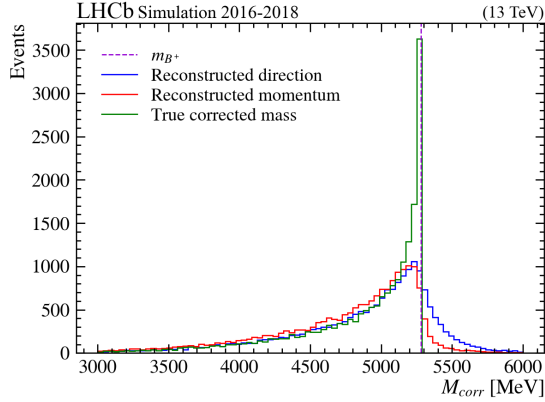


Figure 8.4: Comparison of M_{corr} distributions for the reconstructed momentum and direction with the true values of the $B^+ \rightarrow \mu^+ \nu_\mu e^+ e^-$ decay given by the MC simulation.

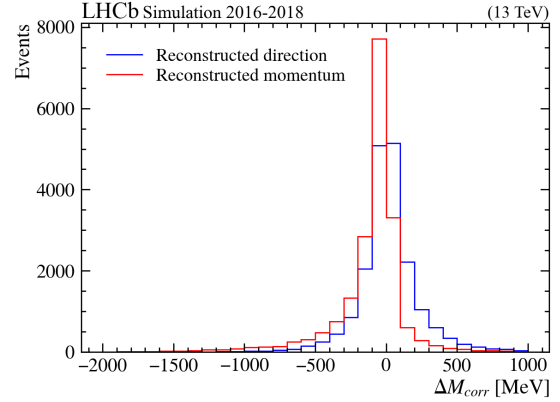


Figure 8.5: ΔM_{corr} between M_{corr} for reconstructed momentum or direction and the true values of M_{corr} of the $B^+ \rightarrow \mu^+ \nu_\mu e^+ e^-$ decay given by the MC simulation.

8.2 Reference channel

To estimate the number of $B^+ \rightarrow \mu^+ \nu_\mu e^+ e^-$ events in data, the response of the detector has to be taken into account. For this reason, well-known and well-measured decays are used, to compare with the signal. As is presented in Section 6.1 the chosen reference channel for this work is the $B^+ \rightarrow K^+ J/\psi(e^+ e^-)$ decay. The reference channel is selected with the use of the B23MuNu_MueeFake stripping line, which has a prescale of 1%. The processing of the reference channel is done with the same criteria as with the signal channel. In the reference channel, there are no PID requirements for the muon allowing the existence of the kaon.

8.2.1 Dilepton mass measurement

The selection cut applied on the dielectron mass of the reference channel is in the [2650,3300] MeV range, in order to select the J/ψ peak. Figures 8.6 and 8.7 are graphical representations of the distribution and the imposed cut on the dielectron mass of the reference channel.

8.2.2 B^+ invariant mass measurement

Signal candidates with the invariant $K^+ e^+ e^-$ mass in the [5200,5800] MeV range are selected. Here, due to the absence of the neutrino, there is no lost energy. Thus, the corrected mass calculation, as described in equation 6.5 is not needed. So as to mitigate the background from $B^+ \rightarrow K^+ J/\psi$, where the pion is missed, the window is taken with an acceptance $m_{Kee} > 5200$ MeV. The $B^+ \rightarrow K^+ J/\psi$ background contribution can be seen in Fig. 8.9, as the small rise of events around $m_{Kee} > 5200$ MeV. Due to the emission of Bremsstrahlung by high-energy electrons, the dielectron mass of all selected events with m_{ee} in the [2650,3300] MeV range for both data and simulation is being artificially set on the J/ψ mass. This is done so as to overcome the dislocation of the J/ψ signal. Figures 8.8 and 8.9 are graphical representations of the distribution and the imposed window acceptance of the invariant mass

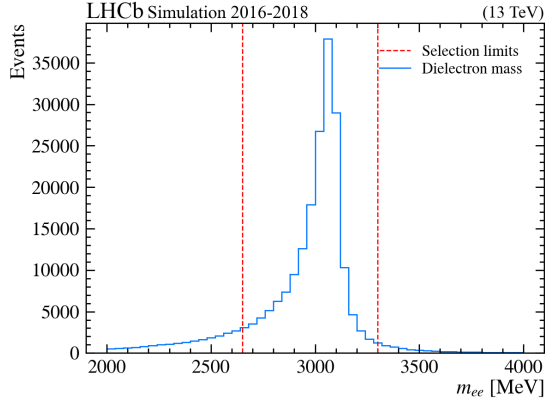


Figure 8.6: m_{ee} distribution of the reference channel and acceptance window in simulation.

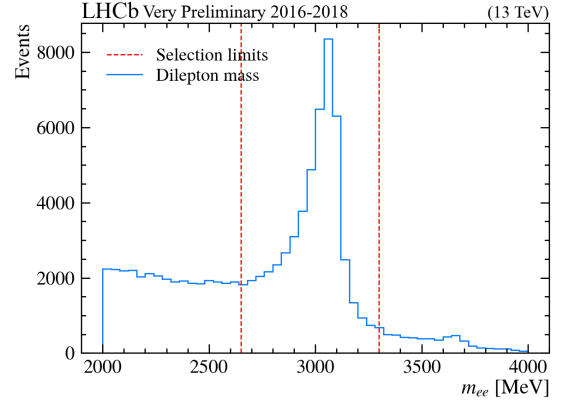


Figure 8.7: m_{ee} distribution of the reference channel and acceptance window in data.

of the $K^+e^+e^-$ final state for both simulation and data.

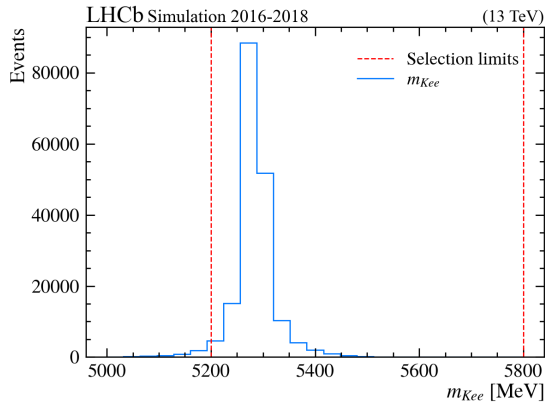


Figure 8.8: m_{Kee} distribution of the reference channel and acceptance window in simulation.

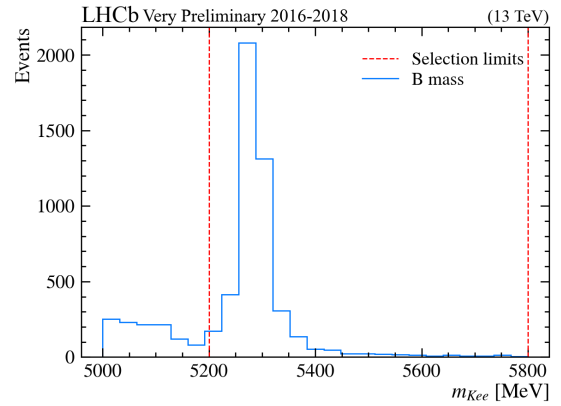


Figure 8.9: m_{Kee} distribution of the reference channel and acceptance window in data.

8.2.3 Data fit

The final step of analysis of the reference channel is fitting the data with a probability density function (PDF). The PDF consists of a weighted sum, i.e. the sum to the PDF is done relative to the signal fraction recorded, of a double-sided Crystal-Ball function for the signal and a decreasing exponential function for the background.

The Crystal Ball function is a probability density function commonly used to model various high-energy physics processes. It consists of a Gaussian core portion and two power-law low-end tails, one at each side of the Gaussian, below certain thresholds, which allows it to adjust for a measurements underestimation by the detector [46]. For the cases of the double-sided Crystal-Ball, a tail exists at either side of the Gaussian core. Of note is, that the left and right parameters do not have to be equal. The equation is given as:

$$f_{\text{Signal}}(x; \alpha_L, n_L, \alpha_R, n_R, \bar{x}, \sigma) = N \cdot \begin{cases} A_L \cdot (B_L - \frac{x-\bar{x}}{\sigma})^{-n_L}, & \text{for } \frac{x-\bar{x}}{\sigma} < -\alpha_L \\ e^{-\frac{(x-\bar{x})^2}{2\sigma^2}}, & \text{for } -\alpha_L \leq \frac{x-\bar{x}}{\sigma} \leq \alpha_R \\ A_R \cdot (B_R - \frac{x-\bar{x}}{\sigma})^{-n_R}, & \text{for } \frac{x-\bar{x}}{\sigma} > \alpha_R \end{cases} \quad (8.1)$$

where A and B stand for:

$$A_{L/R} = \left(\frac{n_{L/R}}{|\alpha_{L/R}|} \right)_{L/R}^n \cdot e^{-\frac{|\alpha_{L/R}|^2}{2}} \quad (8.2)$$

$$B = \frac{n_{L/R}}{|\alpha_{L/R}|} - |\alpha_{L/R}| \quad (8.3)$$

and N is a normalisation factor, with $\alpha_{L/R}, n_{L/R}, \bar{x}$ and σ the parameters fitted in the data.

The function used for the background is given as:

$$f_{\text{Background}} = N \exp(-\lambda x), \quad (8.4)$$

where λ is a dampening constant.

The PDF is given as:

$$f_{\text{PDF}} = s \cdot f_{\text{Signal}} + (1 - s) \cdot f_{\text{Background}}, \quad (8.5)$$

where s is the signal fraction.

The signal PDF is initially fitted on the MC simulation, in order to get the fit shape. Afterward, the $\alpha_{L/R}$ and $n_{L/R}$ parameters were set as fixed on the data fit. The μ and σ parameters were allowed to float in the fit to the data, so to account for any data-simulation differences. Figure 8.10 shows the signal shape according to the MC, with Tab. 8.1 being a summary of the fixed-fitted shape parameters. Figure 8.11 shows the fit of equation 8.5 in the selected data region of Figure 8.9. Table 8.2 lists the fitted parameters with their uncertainties.

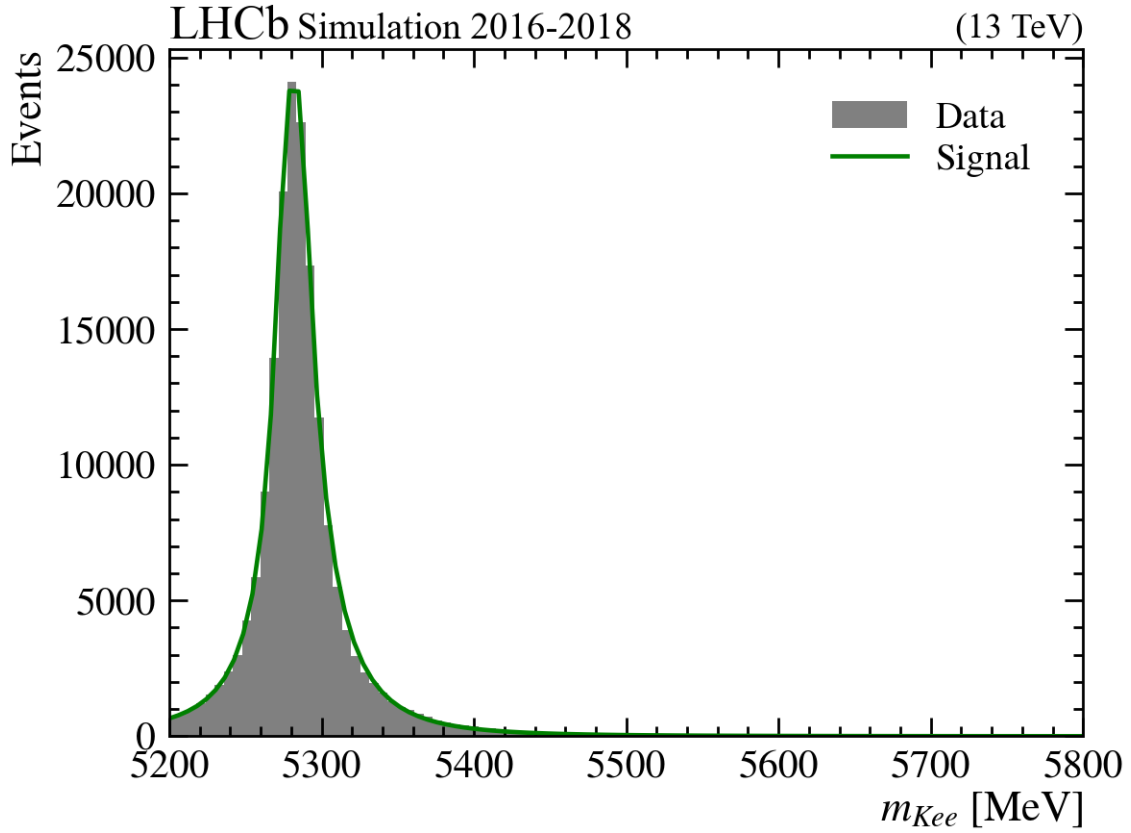


Figure 8.10: Signal shape of the total Run 2 2016-18 $B^+ \rightarrow K^+ J/\psi(e^+e^-)$ decay simulation.

Table 8.1: Parameters of the fit shape.

Variables	Fit-values	Uncertainty
α_L	1.045	0.018
n_L	2.63	0.10
α_R	0.842	0.010
n_R	3.90	0.05

Table 8.2: Results of the fit parameters.

Variables	Fit-value	Uncertainty
\bar{x} [MeV]	5281.87	0.34
σ [MeV]	13.6	0.4
s	0.933	0.012
λ	$3.1 \cdot 10^{-3}$	$0.8 \cdot 10^{-3}$
Signal yield [Events]	4330	90
Background yield [Events]	310	60

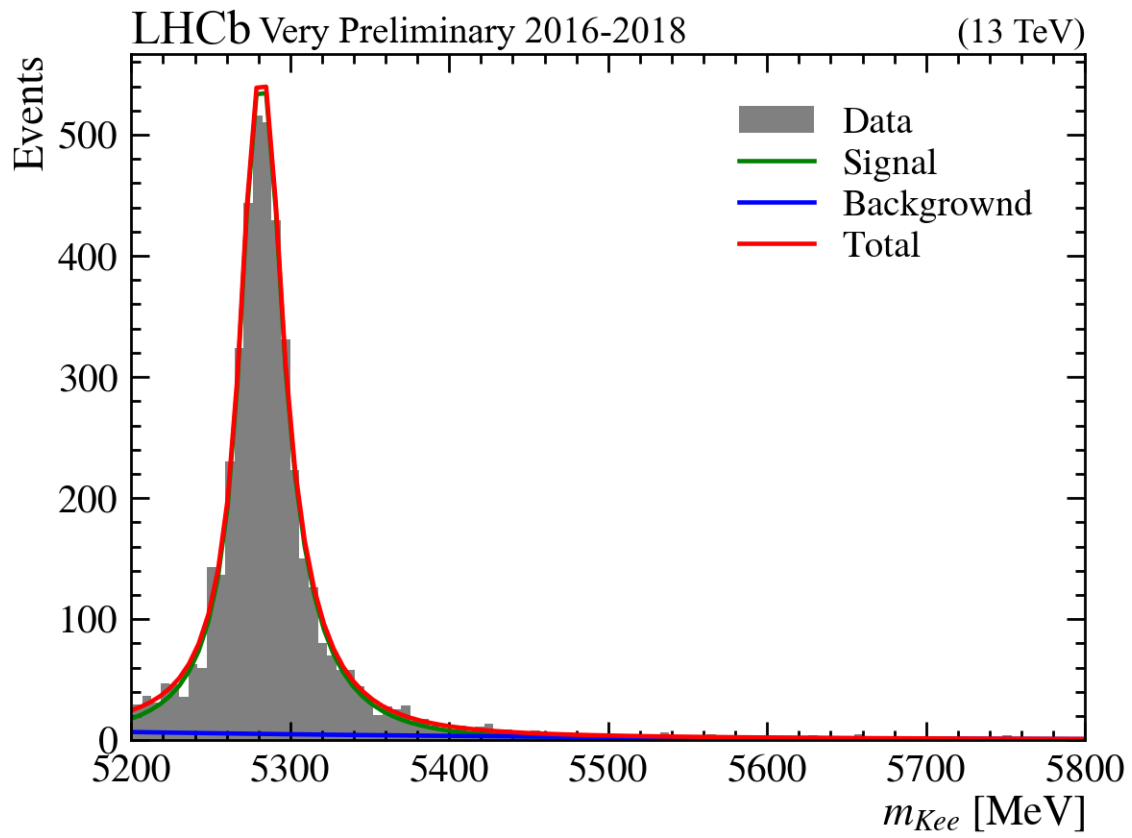


Figure 8.11: Fit of the total Run 2 2016-18 $B^+ \rightarrow K^+ J/\psi(e^+e^-)$ decay data.

8.3 Results

Using all the information from the Sections above, the following quantities can be extrapolated:

- $N_{KJ/\psi(ee)} = 4360 \pm 90$ events, for which the value is derived from the fit of Fig. 8.11, and the error from the square root of the expected value.
- $\mathcal{BR}(B^+ \rightarrow \mu^+ \nu_\mu e^+ e^-) = (2.7 \pm 0.6) \cdot 10^{-8}$, for which the value and error were taken from [36] and adjusted to the kinematics of this study. Specifically the predicted branching ratio is integrated in the m_{ee} region [600, 1000] MeV.
- $\mathcal{BR}(B^+ \rightarrow K^+ J/\psi) \cdot \mathcal{BR}(J/\psi \rightarrow e^+ e^-) = (5.71 \pm 0.032) \cdot 10^{-2}$, for which the value and error are derived from the PDG ³¹.
- $\epsilon_{\text{tot}B^+ \rightarrow \mu^+ \nu_\mu e^+ e^-} = (99.0 \pm 1.6) \cdot 10^{-5}$, for which the value and error are derived from equations 6.3 and 6.4, where as $N_{\text{SelectedEventsInSimulation}}$ the events within the acceptance window presented in Fig. 8.3 and $\epsilon_{\text{generator}}$ the efficiency given by the MC simulation.
- $\epsilon_{\text{tot}(B^+ \rightarrow K^+ J/\psi(e^+ e^-))} = (624.3 \pm 1.5) \cdot 10^{-5}$, for which the value and error are derived from equations 6.3 and 6.4, where as $N_{\text{SelectedEventsInSimulation}}$ the events within the acceptance window presented in Fig. 8.8 and $\epsilon_{\text{generator}}$ the efficiency given by the MC simulation.

This results in $N_{\text{sig}} = (0.30 \pm 0.07)$, which needs to be adjusted by the prescale factor of $\times 100$ implemented on the totality of the reference channel data, giving the final result of:

$$N_{\mu\nu ee} = (30 \pm 7) \text{ events.} \tag{8.6}$$

³¹2016 version

Chapter 9

Discussion

An estimation of the number of events $B^+ \rightarrow \mu^+ \nu_\mu e^+ e^-$ expected to be observed in the 2016-18 LHCb data set is presented in this thesis. For this prediction a comparison of the branching ratios of this decay and of the reference channel $B^+ \rightarrow K^+ J/\psi(e^+ e^-)$ is used, using data and MC simulations taken in the LHCb Run 2 2016-18 framework. All data sets were recorded at an LHCb-specific integrated luminosity of 5.4 fb^{-1} and a center-of-mass-energy of $\sqrt{s} = 13 \text{ TeV}$ [20].

To perform the work, a MC simulation of the $B^+ \rightarrow \mu^+ \nu_\mu e^+ e^-$ decay is used, based on the model from [35]. This initial model, however, did not describe the photon pole of the m_{ee} accurately, as per its erratum [47]. The model significantly overestimated the photon pole, as shown in Fig. 8.2, giving an unphysical result. This is compared to the model presented in [36], which predicted a different branching ratio, with far fewer events in the photon pole. Nevertheless, despite the differences between the models in the photon pole, the two models agree on the number of predicted events around the ρ resonance. A repetition of this work with the new model, from [36] could be of interest, however, the results are expected not to deviate significantly. The two models are very similar in the region of m_{ee} that is selected and therefore the effect on ϵ_{sel} is expected to be small because the selection is done in the ρ resonance. Moreover, because the two signals have different branching ratios, but similar expectations around the ρ resonance, the branching ratio of the newer model [36] is used for the calculation of the $N_{\mu\nu ee}$.

In the study on the reference channel $B^+ \rightarrow K^+ J/\psi(e^+ e^-)$ the primary source of uncertainty stems from the statistical nature of the fit. The results of the analysis of the reference channel are also in agreement with other LHCb studies [45].

In order to estimate the $B^+ \rightarrow \mu^+ \nu_\mu e^+ e^-$ events in data the equation:

$$N_{\mu\nu ee} = N_{Kee} \cdot \frac{\mathcal{BR}(B^+ \rightarrow \mu^+ \nu_\mu e^+ e^-)}{\mathcal{BR}(B^+ \rightarrow K^+ J/\psi) \cdot \mathcal{BR}(J/\psi \rightarrow e^+ e^-)} \cdot \frac{\epsilon_{\text{tot}B^+ \rightarrow \mu^+ \nu_\mu e^+ e^-}}{\epsilon_{\text{tot}(B^+ \rightarrow K^+ J/\psi(e^+ e^-))}},$$

is used, as described in more detail in Section 6.1. The total number of $B^+ \rightarrow \mu^+ \nu_\mu e^+ e^-$ events predicted to be found in LHCb Run 2 data, for the years 2016-18 is:

$$N_{\mu\nu ee} = (30 \pm 7) \text{ events.}$$

This result has a relatively high uncertainty of 23%. This uncertainty has experimental components as well as theoretical ones.

For starters, the estimation method itself has various uncertainties as explained in Section 6.1. The absence of the muon in the reference channel's final state, as well as the different m_{ee} selection regions of the two channels, have an impact on the efficiency quotients. Unfortunately, the peculiarities of the signal decay, do not offer many available reference channels, that would mitigate this large number of small effects. These experimental uncertainties are contributions from systematic uncertainties on the measurements and statistical from the analysis process. Some systematic uncertainties are expected due to the differences between the two decays but they have not been fully calculated yet. A study on the precise evaluations of these systematic uncertainties is set to take place in the future.

As seen also in Section 8.3 the greatest error contribution in this estimate stems from the $\mathcal{BR}(B^+ \rightarrow \mu^+ \nu_\mu e^+ e^-)$ prediction. This is to be expected since it is a value derived from [36] adjusted for this study's kinematic range. There are many sources for this theoretical uncertainty. The dominant uncertainties for the branching ratio prediction are related to the existence of the ρ and ω resonances, and specifically their form factors. An additional uncertainty contribution stems from the V_{ub} element of the CKM matrix.

The result suggests, that the acceptable background in this decay should be at most 70 events, to have a measuring significance of $> 3\sigma$ ³². Here, it is important to stress, that this is the first attempt of a search of this particular decay, making a comparative judgment of the result not possible.

Building upon these findings, the next steps of this study will focus on the background analysis of this event. Calculating and predicting the many backgrounds of the $B^+ \rightarrow \mu^+ \nu_\mu e^- e^+$ decay can be difficult. Similar to estimating the expected signal, an estimation of the number of background events has to be conducted. The development of machine learning classifiers, to reduce the existing background, may be needed to forward this study. Finally, a fit should be set up to the corrected mass distribution with a model of the shapes for both background and signal similar to what was done in the $B^+ \rightarrow \mu^+ \nu_\mu \mu^- \mu^+$ decay paper [44].

All in all this work shows the difficulty, of detecting and studying the $B^+ \rightarrow \mu^+ \nu_\mu e^- e^+$ decay, due to its low statistics, the existence of a neutrino in the final state and the emission of Bremsstrahlung from electrons. Even so, this decay has never been studied before, so setting an upper limit on the branching ratio can be a step to gaining insight into this process. Additionally, taking into account the most recent LHCb upgrade, one can be optimistic about the future study of this decay. The main challenge in the study of the $B^+ \rightarrow \mu^+ \nu_\mu e^- e^+$ decay stems from its low statistics. In future Runs of the experiment, with a higher instantaneous luminosity, this limitation could be suppressed. Lastly, the removal of the L0 trigger on future Runs could remove a further cut on the number of signal candidates.

³²For zero background events the significance comes up to approx. 5σ

Bibliography

- [1] Emi Kou, Phillip Urquijo, W Altmannshofer, F Beaujean, G Bell, M Beneke, II Bigi, F Bishara, M Blanke, C Bobeth, et al. The belle ii physics book. *Progress of Theoretical and Experimental Physics*, 2019(12):123C01, 2019.
- [2] Mark Thomson. *Modern particle physics*. Cambridge University Press, 2013.
- [3] Wikipedia contributors. Standard model — Wikipedia, the free encyclopedia. https://en.wikipedia.org/w/index.php?title=Standard_Model&oldid=1147861546, 2023.
- [4] Atlas Collaboration et al. Observation of a new particle in the search for the standard model higgs boson with the atlas detector at the lhc. *arXiv preprint arXiv:1207.7214*, 2012.
- [5] Cms Collaboration et al. Observation of a new boson at a mass of 125 gev with the cms experiment at the lhc. *arXiv preprint arXiv:1207.7235*, 2012.
- [6] Particle Data Group et al. Review of particle physics. *Chinese Physics C*, 40(10):100001, 2016.
- [7] A Augusto Alves Jr et. al. The LHCb Collaboration. The lhcb detector at the lhc. *Journal of Instrumentation*, 3(08):S08005, aug 2008.
- [8] Lyndon Evans and Philip Bryant. Lhc machine. *Journal of Instrumentation*, 3(08):S08001, aug 2008.
- [9] LHCb Collaboration. Lhcb detector performance. *International Journal of Modern Physics A*, 30(07):1530022, 2015.
- [10] R Aaij, J Albrecht, F Alessio, S Amato, E Aslanides, I Belyaev, M Van Beuzekom, E Bonaccorsi, R Bonnefoy, L Brarda, et al. The lhcb trigger and its performance in 2011. *Journal of Instrumentation*, 8(04):P04022, 2013.
- [11] <https://cerncourier.com/a/moedal-becomes-the-lhcs-magnificent-seventh/>.
- [12] The LHCf Collaboration et. al. The lhcf detector at the cern large hadron collider. *Journal of Instrumentation*, 3(08):S08006, aug 2008.
- [13] The TOTEM Collaboration et. al. The totem experiment at the cern large hadron collider. *Journal of Instrumentation*, 3(08):S08007, aug 2008.

- [14] <https://www.washington.edu/news/2019/03/05/faser-detector-lhc/>.
- [15] M. N. Achasov. Review of results from SND detector. In *AIP Conference Proceedings*. AIP, 2002.
- [16] Georges Aad, JM Butterworth, J Thion, U Bratzler, PN Ratoff, RB Nickerson, JM Seixas, I Grabowska-Bold, F Meisel, S Lokwitz, et al. The atlas experiment at the cern large hadron collider. *Jinst*, 3:S08003, 2008.
- [17] CMS Collaboration, S Chatrchyan, G Hmayakyan, V Khachatryan, AM Sirunyan, W Adam, T Bauer, T Bergauer, H Bergauer, M Dragicevic, et al. The cms experiment at the cern lhc. *Jinst*, 3:S08004, 2008.
- [18] Kenneth Aamodt, A Abrahantes Quintana, R Achenbach, S Acounis, D Adamová, C Adler, M Aggarwal, F Agnese, G Aglieri Rinella, Z Ahammed, et al. The alice experiment at the cern lhc. *Journal of Instrumentation*, 3(08):S08002, 2008.
- [19] Yu Nakahama. The atlas trigger system: Ready for run-2. *Journal of Physics: Conference Series*, 664:082037, 12 2015.
- [20] The LHCb collaboration. LHCb Luminosity Project, 2023.
- [21] <https://home.cern/science/accelerators/accelerator-complex>.
- [22] https://lhcb.web.cern.ch/speakersbureau/html/bb_ProductionAngles.html.
- [23] R Antunes Nobrega, A Franca Barbosa, I Bediaga, G Cernicchiaro, E Correade Oliveira, J Magnin, J Marquesde Miranda, A Massafferri, E Polycarpo, A Reis, et al. Lhcb reoptimized detector design and performance: Technical design report. 2003.
- [24] Hermann Kolanoski and Norbert Wermes. *Particle Detectors: Fundamentals and Applications*. Oxford University Press, USA, 2020.
- [25] Giulia Tuci. Searching for confirmation of charm CP violation in K_S^0 final states at LHCb, 2020. Presented 12 Apr 2021.
- [26] <https://lhcb.physik.uzh.ch/ST/public/material/index.php>.
- [27] Performance of the LHCb outer tracker. *Journal of Instrumentation*, 9(01):P01002–P01002, jan 2014.
- [28] J. Andre, P. Charra, W. Flegel, P.A. Giudici, O. Jamet, P. Lancon, M. Losasso, F. Rohner, and C. Rosset. Status of the lhcb magnet system. *IEEE Transactions on Applied Superconductivity*, 12(1):366–371, 2002.
- [29] M Adinolfi, G Aglieri Rinella, E Albrecht, T Bellunato, S Benson, T Blake, C Blanks, S Brisbane, NH Brook, M Calvi, et al. Performance of the lhcb rich detector at the lhc. *The European Physical Journal C*, 73(5):1–17, 2013.

- [30] Martino Borsato. *Study of the $B^0 \rightarrow K^{*0}e^+e^-$ decay with the LHCb detector and development of a novel concept of PID detector: the Focusing DIRC*. PhD thesis, Paris U., IV, 2015.
- [31] T Head. The lhcb trigger system. *Journal of Instrumentation*, 9(09):C09015, sep 2014.
- [32] <https://lhcb.web.cern.ch/speakersbureau/html/TriggerScheme.html>.
- [33] R. Aaij et.al. Design and performance of the LHCb trigger and full real-time reconstruction in run 2 of the LHC. *Journal of Instrumentation*, 14(04):P04013–P04013, apr 2019.
- [34] Anna Danilina, Nikolay Nikitin, and Konstantin Toms. Rare four leptonic B-mesons decays with a neutrino in final state. *EPJ Web Conf.*, 222:03019, 2019.
- [35] Theoretical analysis of the leptonic decays $B \rightarrow \ell\ell'\bar{\nu}_{\ell'}$, author = Ivanov, Mikhail A. and Melikhov, Dmitri. *Phys. Rev. D*, 105:014028, Jan 2022.
- [36] Stephan Kürten, Marvin Zanke, Bastian Kubis, and Danny van Dyk. Dispersion relations for $B \rightarrow \ell\nu\ell'\ell'+$ form factors. *Phys. Rev. D*, 107(5):053006, 2023.
- [37] M Clemencic, G Corti, S Easo, C R Jones, S Miglioranzi, M Pappagallo, P Robbe, and (on behalf of the LHCb Collaboration). The lhcb simulation application, gauss: Design, evolution and experience. *Journal of Physics: Conference Series*, 331(3):032023, dec 2011.
- [38] <http://lhcbdoc.web.cern.ch/lhcbdoc/boole/>.
- [39] Torbjörn Sjöstrand, Stefan Ask, Jesper R Christiansen, Richard Corke, Nishita Desai, Philip Ilten, Stephen Mrenna, Stefan Prestel, Christine O Rasmussen, and Peter Z Skands. An introduction to pythia 8.2. *Computer physics communications*, 191:159–177, 2015.
- [40] David J Lange. The evtgen particle decay simulation package. *Nuclear Instruments and Methods in Physics Research Section A: Accelerators, Spectrometers, Detectors and Associated Equipment*, 462(1-2):152–155, 2001.
- [41] <http://lhcbdoc.web.cern.ch/lhcbdoc/decfiles/>.
- [42] Piotr Golonka and Zbigniew Was. Photos monte carlo: a precision tool for qed corrections in z and w decays. *The European Physical Journal C-Particles and Fields*, 45(1):97–107, 2006.
- [43] Sea Agostinelli, John Allison, K al Amako, John Apostolakis, H Araujo, Pedro Arce, Makoto Asai, D Axen, Swagato Banerjee, GJNI Barrand, et al. Geant4—a simulation toolkit. *Nuclear instruments and methods in physics research section A: Accelerators, Spectrometers, Detectors and Associated Equipment*, 506(3):250–303, 2003.
- [44] R. Aaij et.al. Search for the rare decay $B^+ \rightarrow \mu^+\nu\mu^+\mu^-$. aug 2019.

- [45] Measurement of lepton universality parameters in $B^+ \rightarrow K^+ \ell^+ \ell^-$ and $B^0 \rightarrow K^{*0} \ell^+ \ell^-$ decays. 12 2022.
- [46] Tomasz Skwarnicki. *A study of the radiative CASCADE transitions between the Upsilon-Prime and Upsilon resonances*. PhD thesis, Cracow, INP, 1986.
- [47] Mikhail A. Ivanov and Dmitri Melikhov. Erratum: Theoretical analysis of the leptonic decays $B \rightarrow \ell \ell' \bar{\nu}_{\ell'}$ [Phys. Rev. D 105, 014028 (2022)]. *Phys. Rev. D*, 106:119901, Dec 2022.

List of Figures

2.1	Standard Model. Figure taken from [3].	8
3.1	The first-order Feynmann diagrams of the $B^+ \rightarrow \mu^+ \nu_\mu e^+ e^-$ decay. By ignoring the $\gamma - e^- - e^+$ vertex one gets the first-order diagrams of the $B^+ \rightarrow \mu^+ \nu_\mu \gamma$ decay.	12
4.1	The LHC and the CERN accelerator complex [21].	14
4.2	Pseudorapidity distributions of $b\bar{b}$ as produced in the LHC. The red box signifies the acceptance of the LHCb detector, while the yellow the acceptance of a detector with cylindrical geometry. The plot is generated using MC simulation for Run 2. The Figure is taken from [22].	15
4.3	The LHCb detector in Run 2 with its sub-detectors. [23]	16
4.4	The VELO sub-detector. Figure taken from [7]	18
4.5	Trigger Tracker x-u-v-x configuration. Figure taken from [26].	18
4.6	IT layout. Figure taken from [26]	19
4.7	(a) Module cross section.(b) Arrangement of OT straw-tube modules in layers and stations. Figure taken from [27]	19
4.8	The LHCb magnet. Figure from [28].	20
4.9	Cherenkov angle in the C_4F_{10} radiator of RICH1. Figure from [9]	21
4.10	Layout of the vertical RICH1 detector. Figure from [23].	22
4.11	Distribution of E/pc in the ECAL for electrons (red) and hadrons (blue), obtained from data recorded in 2011. Figure from [9].	24
4.12	Schematic representation of Bremsstrahlung photons emitted by an electron before and after the magnet. Figure taken from [30].	25
4.13	Side view of the muon system. Figure from [7]	26
4.14	Illustration of the triggering process in LHCb during Run2 (year: 2015). Figure from [32].	27
5.1	Virtual-photon emitted from the light quark of the B meson. Figure taken from [34]	30
5.2	Virtual-photon emitted from the heavy quark of the B-meson. Figure taken from [34].	31
5.3	Virtual-photon emitted from the lepton in the final state. Figure taken from [34].	32

5.4	Graphical representation of the θ_γ , θ_W and ϕ angles, where the denotion ℓ stands for muons and the denotion ℓ' stands for electrons. Figure provided by Fabian Glaser.	33
6.1	Comparison of the M_{corr} and $M_{\mu ee}$	37
7.1	Destruction of the M_{corr} for events with zero, one, and more than one Bremsstrahlung photons.	40
7.2	Comparison of $B^+ \rightarrow \mu^+ \nu_\mu e^+ e^-$ candidates in simulation with and without running DiElectronMaker in the production of nTuples.	41
7.3	Variation in the number of Bremsstrahlung photons attributed to an event after the application of the DElectronMaker.	41
8.1	M_{corr} distribution of the signal, π^0 and η modes.	44
8.2	m_{ee} distribution of the signal, π^0 and η modes.	44
8.3	Corrected mass of the B^+ meson, of the $B^+ \rightarrow \mu^+ \nu_\mu e^+ e^-$ decay in simulation.	45
8.4	Comparison of M_{corr} distributions for the reconstructed momentum and direction with the true values of the $B^+ \rightarrow \mu^+ \nu_\mu e^+ e^-$ decay given by the MC simulation.	46
8.5	ΔM_{corr} between M_{corr} for reconstructed momentum or direction and the true values of M_{corr} of the $B^+ \rightarrow \mu^+ \nu_\mu e^+ e^-$ decay given by the MC simulation.	46
8.6	m_{ee} distribution of the reference channel and acceptance window in simulation.	47
8.7	m_{ee} distribution of the reference channel and acceptance window in data.	47
8.8	m_{Kee} distribution of the reference channel and acceptance window in simulation.	47
8.9	m_{Kee} distribution of the reference channel and acceptance window in data.	47
8.10	Signal shape of the total Run 2 2016-18 $B^+ \rightarrow K^+ J/\psi(e^+ e^-)$ decay simulation.	49
8.11	Fit of the total Run 2 2016-18 $B^+ \rightarrow K^+ J/\psi(e^+ e^-)$ decay data.	50

List of Tables

2.1	Relative strength of forces: The three fundamental interactions relative to particle physics. The relative strengths are approximate indicative values for two fundamental particles at a distance of 1 fm = 10^{-15} m (roughly the radius of a proton). All numbers were taken from [2].	9
4.1	Summary of the different L0 thresholds in Run2. All numbers were taken from [33].	27
7.1	Summary of the preselection criteria for the $B^+ \rightarrow \mu^+ \nu_\mu e^+ e^-$ decay.	42
7.2	Vetoos placed on the $B^+ \rightarrow \mu^+ \nu_\mu e^+ e^-$ decay data.	42
8.1	Parameters of the fit shape.	49
8.2	Results of the fit parameters.	49

Acknowledgments

I am deeply grateful to Prof. Dr. Stephanie Hansmann-Menzemer for providing me with the opportunity to work in her research group during my practical internship and thesis. Her guidance, feedback, and support have been invaluable throughout the entire process.

I want to extend my gratitude to Prof. Dr. Klaus Reygers for agreeing to be my second examiner in my thesis.

I would also like to express my appreciation to my supervisor Dr. Martino Borsato, who introduced me to the fascinating world of flavor physics and mentored me throughout the research process. I am proud to have him as a mentor and friend. Furthermore, I want to acknowledge the other members of the B2munee subgroup, Fabian Glaser and Tom Wolf, for their assistance and collaboration during the research work.

I am also thankful to my teachers and mentors since school, Dr. Stavros Savvas and Dr. Sofokles Sotiriou for their support during my academic journey. Without their guidance and endorsement, I would not have been able to pursue my passion for physics at Heidelberg University. I would like to acknowledge my friends and family for their unwavering support, which has been a source of strength and motivation.

I would like to conclude by dedicating this thesis to two important figures in my life. Firstly, my mom, whose unwavering love and support have been a guiding light in my life. Secondly, I would like to honor my grandfather, who played a fatherly role in my life after I lost my dad at a young age. His guidance and support have been invaluable to me, and I am forever grateful to have him in my life.

Once again, I am grateful to everyone who has contributed to my academic journey and to the successful completion of this thesis. Thank you all.

Erklärung

Ich versichere, dass ich diese Arbeit selbstständig verfasst und keine anderen als die angegebenen Quellen und Hilfsmittel benutzt habe.

Heidelberg, den 12.06.2023

Antonios Kontopoulos

A handwritten signature in black ink, appearing to read 'Kontopoulos', written in a cursive style with a long horizontal stroke at the end.